

## Interstellar and Ejecta Dust in the Cas A Supernova Remnant

Richard G. Arendt<sup>1,2</sup>, Eli Dwek<sup>2</sup>, Gladys Kober<sup>2,3</sup>, Jeonghee Rho<sup>4,5</sup>, and Una Hwang<sup>6,7</sup>

### ABSTRACT

Infrared continuum observations provide a means of investigating the physical composition of the dust in the ejecta and swept up medium of the Cas A supernova remnant. Using low resolution *Spitzer* IRS spectra (5–35  $\mu\text{m}$ ), and broad-band *Herschel* PACS imaging (70, 100, and 160  $\mu\text{m}$ ), we identify characteristic dust spectra, associated with ejecta layers that underwent distinct nuclear burning histories. The most luminous spectrum exhibits strong emission features at  $\sim 9$  and 21  $\mu\text{m}$  and is closely associated with ejecta knots with strong Ar emission lines. The dust features can be reproduced by magnesium silicate grains with relatively low Mg to Si ratios. Another dust spectrum is associated with ejecta having strong Ne emission lines. It has no indication of any silicate features, and is best fit by  $\text{Al}_2\text{O}_3$  dust. A third characteristic dust spectrum shows features that are best matched by magnesium silicates with a relatively high Mg to Si ratio. This dust is primarily associated with the X-ray emitting shocked ejecta, but it is also evident in regions where shocked interstellar or circumstellar material is expected. However, the identification of dust composition is not unique, and each spectrum includes an additional featureless dust component of unknown composition. Colder dust of indeterminate composition is associated with emission from the interior of the SNR, where the reverse shock has not yet swept up and heated the ejecta. Most of the dust mass in Cas A is associated with this unidentified cold component, which is  $\lesssim 0.1 M_\odot$ . The mass of warmer dust is only  $\sim 0.04 M_\odot$ .

*Subject headings:* dust, extinction — infrared: ISM — ISM: individual (Cassiopeia A) — supernova remnants

---

<sup>1</sup>CRESST, University of Maryland – Baltimore County, Baltimore, MD 21250, USA; Richard.G.Arendt@nasa.gov

<sup>2</sup>NASA Goddard Space Flight Center, Code 665, Greenbelt, MD 20771, USA

<sup>3</sup>Department of Physics, IACS, Catholic University of America, Washington DC 20064, USA

<sup>4</sup>SETI Institute, 189 Bernardo Ave, Mountain View, CA 94043

<sup>5</sup>SOFIA Science Center, NASA Ames Research Center, MS 211-3, Moffett Field, CA 94035

<sup>6</sup>NASA Goddard Space Flight Center, Code 662, Greenbelt, MD 20771, USA

<sup>7</sup>The Henry A. Rowland Department of Physics and Astronomy, Johns Hopkins University, 3400 N. Charles Street, Baltimore, MD 21218, USA

## 1. INTRODUCTION

Interstellar dust models that fit the average interstellar extinction curve, the diffuse infrared emission and scattering, polarization, and abundance constraints employ a very limited variety of dust compositions, consisting primarily of polycyclic aromatic hydrocarbons (PAHs), graphite or amorphous carbon, and astronomical silicates (Li & Draine 2001; Zubko et al. 2004; Brandt & Draine 2012; Siebenmorgen et al. 2014). Yet observations of the primary sources of interstellar medium (ISM) dust (or at least the metals therein), asymptotic giant branch (AGB) stars and supernovae (SNe), reveal a significantly richer variety of dust compositions. For example, magnesium sulfide (MgS) is inferred from spectral features of pre-planetary nebulae (Omont et al. 1995) with similar features in carbon-rich AGB stars and PNe (Forrest et al. 1981; Hony et al. 2002). Cherchneff (2012) contains a detailed model of the formation of a wide variety of molecules and dust in an AGB star. More directly, presolar grains of supernova or stellar origin, such as silicate carbide (SiC), silicon nitride (Si<sub>3</sub>N<sub>4</sub>), and aluminum-, calcium- and titanium-oxides are found as meteoritic inclusions (e.g. Zinner 2008). The absence of a wide variety of specific compositions in interstellar dust models indicates that these compositions are not required for fitting various manifestations of dust in the general ISM, either because of their low abundance relative to silicates and carbonaceous dust, or due to the fact that they may have been processed in the ISM.

Supernovae can be important sources of interstellar dust. They produce all the refractory elements needed for the formation of dust, and their ejecta largely retain the compositional inhomogeneity of the progenitor star. They may therefore be sources of dust with unusual chemical and isotopic compositions. Furthermore, SNe are drivers of the chemical evolution in galaxies, and therefore potentially the most important sources of interstellar dust. In young populations before low mass stars have evolved off the main sequence, e.g. high redshift galaxies, SNe are the dominant source of thermally-condensed dust, though additional grain growth by cold accretion within dense clouds may be required to explain the inferred dust mass in these systems (Dwek & Cherchneff 2011; Valiante et al. 2011). Determining the mass and composition of SN condensed dust is therefore key for understanding the origin, evolution, and processing of dust in galaxies.

The Cas A remnant is an ideal object for studying the composition and abundance of dust that formed in the ejecta of a core collapse SN. The SN was not definitively recorded at the time that it occurred. Studies of the expansion of the supernova remnant (SNR) estimate that the explosion was in the year 1681±19 (Fesen et al. 2006). Yet fortunately, light echoes of the Cas A SN have allowed studies of this old event with modern instruments. Such observations have revealed that Cas A was a Type IIb SN (Krause et al. 2008) with distinct asymmetry in its explosion (Rest et al. 2011). Dynamical and compositional asymmetries are still imprinted on the Cas A SNR today, but the dominant structure of the Cas A SNR is characterized by a clear distinction between the forward shock sweeping up the interstellar (and/or circumstellar) medium, and the reverse shock through which the SN ejecta is expanding.

The ejecta consists of three main components: the first, containing most of the mass, is a low

density phase that is heated by the reverse shock to X-ray emitting temperatures ( $\gtrsim 10^6$  K). The second component consists of dense fast-moving knots (FMKs) that have gone through the reverse shock, and are radiatively cooling by line emission at optical and infrared (IR) wavelengths. A third component comprises ejecta that has not yet encountered the reverse shock, and is primarily heated by the ambient radiation within the SNR interior.

In this paper we revisit the analysis of the mid- to far-IR spectra of the dust in Cas A. IR emission can arise from dust in each of the ejecta components discussed above, as well as the circumstellar medium (CSM) or ISM that is shocked by the advancing SN blast wave, i.e. the forward shock. Our main goal is to separate and identify different types of dust that associated with different ejecta (and ISM or CSM) components and to determine the spatial distribution of the different types of dust. Our approach will provide important information on the physical processes that facilitate or inhibit the nucleation of dust in the different layers of the ejecta, the resulting dust composition, and the dust heating mechanisms that give rise to the IR emission. Our approach is different from previous ones (Ennis et al. 2006; Rho et al. 2008) which only grouped the IR emission into distinct spectral components, with no relation to the nature of the ejecta from which they originated.

The outline of our analysis is:

- (1) We identify a set of *spatial templates* that are used as the initial indicators of regions of different ejecta composition and/or physical conditions around the SNR. These are illustrated in Figure 1, with the details of their derivation in the Appendix.
- (2) For each spatial template, we identify *zones* (subregions) where that template is most prominent with respect to the other templates. These are described in Section 3.1 and shown in Figure 2.
- (3) Within each of the zones and at each wavelength, we use the spatial correlation between the data and the template (see Eq. 1) to derive the *characteristic spectra* associated with each spatial template. These are presented in Section 3.1 and Figure 3. Analysis of these characteristic spectra provides indications of the dust composition and temperature(s).
- (4) Finally, at each spatial location across the entire SNR, the spectrum is decomposed as a linear combination of the characteristic spectra. The coefficients of these decompositions are mapped out to reveal images of the *spatial distributions* of the dust that gives rise to each characteristic spectrum. This is described in Section 3.2 and illustrated in Figure 4.

Section 2 of this paper describes the preparation of the *Spitzer* IRS data to create a spectral cube of the dust continuum emission of Cas A. Section 3 explains the data analysis steps described above, with the details and results of modeling the characteristic spectra presented in Section 4. In Section 5 we discuss the results, including what conclusions can and cannot be drawn concerning the dust composition and mass. The work is summarized in section 6.

## 2. DATA PREPARATION

Our work began with the low resolution IRS spectral data cubes used by Rho et al. (2008). There are 4 cubes, generated from the 1st and 2nd order spectra in short and long wavelength low resolution modules. At each wavelength, the data were convolved to the spatial resolution at the longest IRS wavelength,  $38.33 \mu\text{m}$ , using kernels derived from Tiny Tim / Spitzer (STINYTIM)<sup>7</sup> PSFs according to Gordon et al. (2008). The three shorter wavelength cubes were then reprojected to the same scale and orientation as the longest wavelength (SL1) cube. The data are then combined into a single IRS low-resolution cube covering  $5 - 38 \mu\text{m}$  with a fixed spatial resolution. Weighted averages were used at the wavelengths that overlap between the different spectral orders and modules.

For the purpose of analyzing the dust emission, we created a continuum spectral cube by replacing all the emission lines with smooth polynomial fits to the continuum on either side of each line. This procedure is performed independently for each spatial pixel of the cube and each line. It avoids any need to fit the lines themselves, which can be found at various velocity components at each pixel because of the high expansion velocities of Cas A. The lines that were thus removed are listed in the row and column headings of Table 1. Finally, to remove remaining artifacts and improve the signal to noise, the continuum cube was smoothed in wavelength to a spectral resolution of  $R = \lambda/\Delta\lambda \approx 20$ , and trimmed to a maximum wavelength of  $35 \mu\text{m}$ . After this smoothing, there are only  $\sim 40$  truly independently-sampled wavelengths in the data cube.

Longer wavelength information was obtained by using *Herschel* PACS (Pilbratt et al. 2010; Poglitsch et al. 2010) observations at  $70, 100, \text{ and } 160 \mu\text{m}$ , with the appropriate spatial convolution of the  $70$  and  $100 \mu\text{m}$  images whose native resolution is better than the IRS at  $38 \mu\text{m}$ . (All *Herschel* data used here were Level 2 products generated from Standard Product Generation SPG 4.1.0.) At  $160 \mu\text{m}$  the SNR is substantially confused by ISM emission. This confusion was reduced by subtracting an empirically scaled version of the *Herschel* SPIRE (Griffin et al. 2010)  $250 \mu\text{m}$  image in which the synchrotron emission of the SNR was subtracted by extrapolation from the  $350$  and  $500 \mu\text{m}$  bands. The subtraction is an improvement, but is still imperfect, in part due to the lower spatial resolution of the longer wavelength SPIRE data.

The synchrotron emission is removed from the final *Spitzer* continuum cube by subtraction of the VLA radio template (DeLaney 2004) extrapolated assuming a power law spectrum  $S_\nu \sim \nu^{-0.71}$ .

---

<sup>7</sup><http://irsa.ipac.caltech.edu/data/SPITZER/docs/dataanalysisistools/tools/contributed/general/stinytim/>

### 3. ANALYSIS

#### 3.1. Derivation of Characteristic Spectra

One of the primary goals of this analysis was to find the continuum spectra of dust that is found in regions of various physical parameters and compositions throughout the SNR. The regions to be investigated are identified via six distinct spatial templates. These templates are shown in Figure 1 and Table 2, and are described in more detail in the Appendix. To identify the spectra associated with each of the six emission templates, we superimposed all the templates and for each one we identified the zones where its relative emission was the dominant component. Because of the strong and widespread [Ar II] emission, in some cases the zones necessarily included [Ar II] emission as well. The zones selected for each of the templates are outlined in Figure 2.

For all pixels,  $i$ , of each zone of the 6 selected emission templates,  $T_j(i)$ , the data  $D(i, \lambda)$  can be represented by:

$$D(i, \lambda) = \sum_{j=1}^6 S_j(\lambda)T_j(i) + C(\lambda). \quad (1)$$

The parameters  $C(\lambda)$ , a constant term (which should be small) to account for errors in the background levels, and  $S_j(\lambda)$ , the spectra associated with each of the templates, can thus be derived via a least-squares fit or linear regression between the data and the templates.

For the Ar II zone, the sum is strongly dominated by this template, and  $S_{ArII}(\lambda)$  is determined as the slope of a linear least squares fit between  $D(i, \lambda)$  and  $T_{ArII}(i)$ . Some Ar II emission is unavoidable in all other zones, therefore for the other zones the spectra  $S_j(\lambda)$  were derived using a linear regression between  $D(i, \lambda)$  and two templates:  $T_j(i)$  and  $T_{ArII}(i)$ . The characteristic spectra derived are shown in Figure 3.

When these derived spectra are multiplied by the spatial templates over the entire SNR (not just within the selected zones) and the result is subtracted from the data cube, we found that there was one region of residual emission that was particularly strong and consistently positive at all wavelengths. This region is in the south central portion of the SNR. One additional zone was created to cover this region (the “South Spot” in Fig. 2), and the measured spectrum within this zone is included in Fig. 3.

The characteristic spectra are key data that allow detailed examination of the nature of the dust in different regions of the SNR. The modelling and analysis of the characteristic spectra are presented in Section 4.

#### 3.2. Spatial Distributions of the Characteristic Spectra

In principle, the spatial templates,  $T_j(i)$  and their characteristic spectra,  $S_j(\lambda)$ , provide a complete description of the continuum data cube. However, because the characteristic spectra were

derived only from limited zones of the SNR, it is informative to revisit the data modelling given by Equation (1), but this time we use the seven  $S_j(\lambda)$  characteristic spectra as known quantities, and solve for the spatial distributions,  $I_j(i)$ , of each spectrum over the entire SNR.

$$D(i, \lambda) = \sum_{j=1}^7 S_j(\lambda) I_j(i) + C(i) \quad (2)$$

In this fitting, a constant term,  $C(i)$ , is still present to account for background errors, but now this constant is a function of position rather than wavelength. If the characteristic spectra are uniquely and perfectly correlated with the spatial templates, then we should find that the spatial distributions are identical to the templates,  $I_j(i) = T_j(i)$ . Differences between the initial templates and these derived spatial distributions would identify (a) regions where the template emission is present, but not accompanied by the characteristic spectrum, and (b) regions where emission matching a characteristic spectrum is present but without corresponding emission of the initial template.

The derived spatial distributions of the different characteristic spectra are shown in Figure 4. Comparison with Figure 1 shows that the derived spatial distribution of the dust associated with Ar II emission is very similar to the input template,  $I_{ArII}(i) \approx T_{ArII}(i)$ . Differences are more evident for dust associated with Ne II and X-ray Fe emission. Yet in both cases the brightest portions of the derived spatial distributions do follow the original templates, even in areas that were outside of the zones where the characteristic spectra were derived. The spatial distribution of the radio dust (i.e. dust associated with the radio template) is very different from original template, as it tends to be concentrated in areas at the periphery of the SNR that are expected to lie between the forward shock and the reverse shock. Material here should be dominated by swept up interstellar or circumstellar material. Interestingly, the spatial distribution identifies a large area on the east side of the SNR which matches the characteristic spectrum, but had not been within the zone used to define that spectrum. The agreement between the Si II dust’s spatial distribution and the initial template is very rough. This spatial distribution is dominated by the morphology of the emission at wavelengths  $\lambda \geq 70 \mu\text{m}$ . The spatial distribution of dust matching the Ar III characteristic spectrum is confined to a few of the brightest peaks in the continuum and [Ar III] images.

Guided by these results, we find that a traditional 3-color image can be constructed to emphasize the different components via the tint of the continuum emission, as shown in Figure 5. This image combines the emission at 11.8, 20.8, and 70  $\mu\text{m}$  from the smoothed continuum data cube. These wavelengths are chosen by selecting those where the characteristic spectra (Fig. 3) have the greatest differences from one another.

### 3.3. Total Emission

Figure 6 shows the seven Cas A characteristic spectra with their actual intensities (i.e. without normalization). The total emission of each is calculated by integrating the characteristic spectra,  $S_j(\lambda)$  (Fig. 3), over the regions of the corresponding spatial distributions,  $I_j(i)$  (Fig. 4). This comparison shows that in the ejecta, the Ar II dust component is dominant at wavelengths from 8 to 35  $\mu\text{m}$ . The dust associated with the radio emission is assumed to be swept up ISM dust rather than ejecta, because of its spatial distribution turns out to be largely confined to the periphery of the SNR. The brightness of the ISM dust is generally  $< 1/3$  of the brightness of the ejecta dust. The sum of the all the spectra is also shown as a “fit” to the total Cas A spectrum as measured directly from *Spitzer* and *Herschel* data. The general agreement at 10 – 35  $\mu\text{m}$  indicates that there are no major missing components. At shorter wavelengths, as the SNR emission drops towards the level of the background and the noise, the comparison is not as good.

## 4. DUST COMPOSITIONS FROM THE CHARACTERISTIC SPECTRA

Six of the seven characteristic spectra (Figure 3) show strong emission at wavelengths from 10 to 40  $\mu\text{m}$ . The *Spitzer* IRS spectra across these wavelengths reveal distinctive features in some of these spectra. The features are suggestive of silicates with peaks of varying sharpness at  $\sim 10$  and  $\sim 20$   $\mu\text{m}$ . In order to identify the particular type of silicates and/or other grain compositions that produce each of the characteristic spectra, we assembled a set of grain absorption efficiencies from published optical constants (Table 3), and fitted each characteristic spectrum,  $S_j(\lambda)$ , as the weighted,  $M_{n,i,j}$ , sum of different grain mass absorption coefficients,  $\kappa_n(\lambda)$ , applied to blackbody emission at different temperatures,  $B(T_i)$ :

$$S_j(\lambda) = \sum_n \sum_{T_i=20\text{K}}^{2000\text{K}} M_{n,i,j} \kappa_n(\lambda) B(T_i) \quad (3)$$

where  $n$  and  $i$  are indices for dust composition and temperature respectively. The mass absorption coefficients,  $\kappa_n(\lambda) \equiv 3Q_n(\lambda, a)/4\rho_n a$ , or more directly the absorption efficiencies,  $Q(\lambda, a)$ , are calculated using Mie theory and assuming a relatively small grain size  $a = 0.01$   $\mu\text{m}$  (e.g. Nozawa et al. 2008, 2010), although  $Q(\lambda, a)/a$  is essentially independent of  $a$  for  $a \lesssim 0.1$   $\mu\text{m}$  at these wavelengths. ( $\rho_n$  is the mass density of grains of composition  $n$ .)

The MPFIT code (Markwardt 2009) was used to determine coefficients  $M_{n,i,j}$  needed to fit each normalized spectrum with the constraint that  $M_{n,i,j} \geq 0$ . In the fitting, the dust temperature is constrained to lie on a grid of values ranging logarithmically from  $T_i = 20$  to  $T_i = 2000$  with  $\Delta \log_{10}(T_i) = 0.05$  ( $0 \leq i \leq 40$ ). Only components with intensities exceeding  $10^{-4}$  times the peak of the fitted spectrum are kept in the final result. For the purpose of fitting, the uncertainties of the characteristic spectra (normalized to a peak of 1.0) were taken to be  $\sigma_S = 0.2S$  with a floor of  $\sigma_S \geq 0.01$ . The 20% fractional uncertainty is chosen to represent both the noise in the

measurement and systematic errors associated with the data reduction (e.g. joining spectral orders, subtracting spectral lines). The 1% (of peak flux) floor on the uncertainties represents the random noise terms, which generally dominate the spectra at  $\lambda \lesssim 10 \mu\text{m}$ . These uncertainties are indicated as the gray bands in Figures 14-20. Given these uncertainties, spectral features at  $\sim 8 - 10$ , 12, and  $\sim 18 - 20 \mu\text{m}$  reflect real features of the dust spectra, but smaller spectral details and details at shorter wavelengths carry little weight in the fitting.

For each spectrum, an initial set of fits was performed using only one dust composition,  $n$ , at a time. No single composition provided a good fit to the spectrum. The fits were repeated using all possible combinations of pairs of compositions (i.e. the left summation in Equation 3 includes only two of the possible values of  $n$ ). Some combinations explored in this way result in substantial improvements in the fits. Usually the improved fits involved the pairing of a dust composition with strong spectral features with another composition that is relatively “featureless.” To check if a second “strong-featured” dust component was warranted, we also performed a set of fits using 3 compositions, but with the constraint that one was required to have a “featureless” emission spectrum. Since all the featureless compositions produce similar results, we fixed either graphite or the “ac” amorphous carbon composition as the required featureless component in these tests.

The quality of the 1- and 2-composition fits as measured by  $\chi^2$  is shown in Figures 7-12. The left panel of each figure shows a matrix of the  $\chi^2$  values, with generalized axes corresponding to different compositions. This is useful to get an overview of which pairs of compositions provide the best fits. The general groupings are based on chemical and/or spectral similarity. The right panel of each of the figures displays the same  $\chi^2$  values but now plotted as a function of the second composition and color coded according to the first composition. This plot quantifies  $\chi^2$  and allows specific compositions to be identified. The results for single composition fits correspond to the upper envelope of the curves in these plots (or the diagonal of the matrix in the left panels). Examples of the best fitting 2- and 3-composition models, as well as contrasting models that also provide reasonably good fits, are shown in Figures 14-20. The results for the 7 different characteristic spectra are discussed in more detail below.

#### 4.1. Ar II Dust

The characteristic dust spectrum associated with Ar II exhibits the sharpest peaks at 9 and 21  $\mu\text{m}$  and has a third, weaker peak at  $\sim 12 \mu\text{m}$ . The astronomical silicate of the typical ISM does not have silicate peaks sharp enough to produce the observed features. Magnesium silicates (particularly  $\text{Mg}_{0.7}\text{SiO}_{2.7}$ , characterized by  $\text{Mg}/\text{Si} = 0.7$ ) have peaks that are in roughly the right locations, but their shapes are not a good match to the data. However, when two-composition fits are performed, the addition of a second component lacking strong spectral features (e.g. graphite, amorphous C, or  $\text{Al}_2\text{O}_3$ ), can soften and smooth the appearance of the silicate peaks to provide a much better fit to the spectrum.



The best 2-component fit (see Figure 14) employs  $\text{Mg}_{0.7}\text{SiO}_{2.7}$  to fit the 9 and 21  $\mu\text{m}$  silicate peaks, and graphite as the featureless component that weakens the relative strength of the peaks. The fit to these peaks is very good, although the weaker 12  $\mu\text{m}$  peak is not fit at all. Despite the overall good fit, the temperature components needed for the Mg silicate are somewhat suspicious. Components at 71–63 K are needed to fit the 21  $\mu\text{m}$  feature, but are too cold to contribute to the 9  $\mu\text{m}$  feature. Conversely a 500 K component produces the 9  $\mu\text{m}$  peak while contributing little to the 21  $\mu\text{m}$  peak. Small, stochastically heated grains might be expected to be heated to this range of temperatures, but it is problematic that there is no indication of grains at intermediate temperatures ( $70 \text{ K} < T < 400 \text{ K}$ ). This suggests that the absorption efficiencies used here are not a true physical representation of the Ar II dust. The actual dust must either have a relatively stronger 9  $\mu\text{m}$  peak so that it can produce the observed spectrum from cooler dust, or it must have a somewhat lower absorption efficiency at roughly 10–20  $\mu\text{m}$  so that the presence of grains at intermediate temperatures would be required.

As suggested by the best 2-component fits, the best 3-component fit combines the  $\text{Mg}_{0.7}\text{SiO}_{2.7}$  with graphite (to weaken the silicate peaks) and adds a nonstoichiometric spinel to provide the 12  $\mu\text{m}$  peak (see Fig. 14). However there is still a tendency in this fit to use distinctly different temperatures and/or compositions to fit each different spectral feature. The spinel material that produces the 12  $\mu\text{m}$  peak is required to be at extremely high temperatures so that it only contributes to this peak. Alternate sources of the 12  $\mu\text{m}$  feature are  $\text{SiO}_2$  and  $\text{SiC}$ . For both of these materials, the spectral features are too sharp and slightly too blue to provide a good match when the mass absorption coefficients,  $\kappa(\lambda)$ , are calculated from Mie theory for spherical grains. However, calculations assuming a continuous distribution of ellipsoids (CDE) for particle shapes (Bohren & Huffman 1983), result in spectral features that are broader and redder. The dust temperatures required to produce the features are also much more reasonable. Figure 14 also shows the fits when CDE calculations are used for a third composition of  $\text{SiO}_2$  or  $\alpha\text{-SiC}$ .  $\text{SiO}_2$  provides some contribution to all three of the observed peaks.  $\text{SiC}$  only provides the 12  $\mu\text{m}$  peak.

## 4.2. Ar III Dust

The Ar III dust spectrum is very similar to that of the Ar II dust. It was derived separately to check if there might be an identifiable shift in dust temperature or composition in these closely related regions. Not surprisingly, the combinations that produced good fits to the Ar II spectrum also produce good fits to the Ar III spectrum (see Figure 15). The increased strength of the 9  $\mu\text{m}$  peak relative to the 21  $\mu\text{m}$  peak would usually suggest warmer dust temperatures in association with the Ar III. However, because the dust features arise largely from separate components of the models, the temperature of the components are largely unchanged, but the relative mass in the hotter components is higher for the Ar III than for the Ar II spectrum.

For the Ar III spectrum we consistently find that the amorphous C (ac) provides a slightly better fit than the graphite that was somewhat preferred for Ar II spectrum. The Ar III spectrum

is also slightly better fit when hibonite ( $\text{CaAl}_{12}\text{O}_{19}$ ) rather than a spinel composition is used as a third component, although if CDE calculations are applied,  $\text{SiO}_2$  and  $\text{SiC}$  can again provide equally good fits as the third component.

### 4.3. Ne II Dust

The dust associated with Ne II exhibits an unusually smooth spectrum. This spectrum excludes significant amounts of warm silicates, but can be fit by compositions with relatively featureless spectra, e.g. graphite, and amorphous carbon. The best fits are found by combining featureless dust with  $\text{Al}_2\text{O}_3$ . The latter component has a very broad emission peak between 10 and 20  $\mu\text{m}$  that improves the fit. Figure 16 shows the fit for an amorphous carbon (be) and  $\text{Al}_2\text{O}_3$  mixture. The fit suggests that some fraction of the  $\text{Al}_2\text{O}_3$  component is fairly warm ( $T \approx 150$  K), while the brightest carbon dust has a temperature of  $\sim 75$  K. A significant cool ( $\sim 40$  K) dust component helps to fit the *Herschel* data at 70 – 160  $\mu\text{m}$ . The model attributes this to  $\text{Al}_2\text{O}_3$ , but this identification is degenerate because neither of these compositions have any characteristic spectral features at these wavelengths. The composition of very cool components cannot be identified very conclusively, because the shape of the spectra are hardly affected by composition.

Figure 16 also shows the best fit model that does not contain  $\text{Al}_2\text{O}_3$ . In this case a non-stoichiometric spinel provides a relatively small perturbation to an otherwise smooth amorphous C spectrum. Amorphous C picks up the intermediate temperature ( $\sim 135$  K) components that account for the bulk of the 10 – 20  $\mu\text{m}$  emission.

Finally, Figure 16 also shows the best 3-component model for the Ne II dust. The addition of  $\text{TiO}_2$  nominally improves the fit over the best 2-component model, but the changes to the spectrum are too minor to suggest that any third component is warranted.

### 4.4. X-Ray Fe Dust

The spectrum of dust associated with the X-ray Fe emission does exhibit apparent silicate peaks at  $\sim 10$  and 20  $\mu\text{m}$ . The 10  $\mu\text{m}$  peak is relatively weak, suggesting a lack of hot silicate grains. As with the Ar II dust, mixing silicate and more featureless emission (e.g. amorphous C) improves the quality of the fit. The preferred silicates here tend to have higher Mg/Si ratios than those that fit the Ar II and Ar III dust. Figure 17 shows the best 2–composition fit. The temperatures for both components are warm,  $T \approx 100 - 112$  K, with additional hot and cold components to account for the short and long wavelength emission. The figure also shows the best 2–component fit that can be obtained without the use of silicate compositions. This marginal fit uses  $\text{Mg}_{0.6}\text{Fe}_{0.4}\text{O}$  to adjust the shape of the model spectrum near 20  $\mu\text{m}$ , but contains no replacement for a 10  $\mu\text{m}$  silicate feature. The best 3–component fit (see Fig. 17) merely adds  $\text{PAH}^+$  emission to reproduce a bump at 8  $\mu\text{m}$  and sharpen the spectral feature at  $\sim 10$   $\mu\text{m}$ . The overall change in  $\chi^2$  is small.

#### 4.5. South Spot Dust

The South Spot spectrum looks rather different than the X-ray Fe spectrum, yet it tends to be best fit by similar dust compositions. Here the temperatures of the components that produce the  $< 20 \mu\text{m}$  emission are higher than those for the X-ray Fe dust. Figure 18 shows the best 2–component fit which uses similar compositions as the X-ray Fe spectrum (cf. Fig. 17). It also shows a marginal fit obtained without the use of silicates, and thus without any component that provides a  $10 \mu\text{m}$  feature in the spectrum. The best 3–component fit (see Fig. 18) uses nonstoichiometric spinel to make minor adjustments to the shape of a good 2–component model.

#### 4.6. Radio (ISM) Dust

As for the X-ray Fe and South Spot spectra, the spectrum associated with the radio emission tends to be best fit with a mix of silicate and featureless dust (Figure 19). A marginal 2–composition fit, in which  $\text{Mg}_{0.1}\text{Fe}_{0.9}\text{S}$  serves as the “featureless” component across the  $10\text{--}20 \mu\text{m}$  part of the spectrum is also shown in Figure 19. The best 3–component fit (see Fig. 19) is not significantly different from the best 2–component fit, using two featureless components instead of one. The last example in Figure 19 shows the best results when dust compositions are restricted to the astronomical silicate, graphite, PAH and  $\text{PAH}^+$ , which are commonly used to fit general interstellar material (e.g. Draine & Lee 1984; Zubko et al. 2004; Draine & Li 2007). The shape of the astronomical silicate’s  $10 \mu\text{m}$  emission peak is not as sharp as the observed spectrum. Cool  $\text{PAH}^+$  emission provides sufficient adjustment to the shape of the silicate spectrum such that the model does not require graphite or neutral PAH components.

#### 4.7. Si II Dust

The Si II dust spectrum essentially contains only the *Herschel* PACS measurements at 70, 100, and  $160 \mu\text{m}$ , with only upper limits on the emission at shorter wavelengths. Because of this lack of detailed spectral information, the spectrum was only fit with single composition dust models. The measured Si II spectrum apparently has a relatively sharp peak compared to a black body spectrum. The best fit is provided by hibonite ( $\text{CaAl}_{12}\text{O}_{19}$ ) which has a broad emission feature at  $\sim 80 \mu\text{m}$  making it an especially good fit to the data. Figure 20 shows the best fit spectrum ( $\text{CaAl}_{12}\text{O}_{19}$ ), and a fit using a more typical Mg silicate ( $\text{Mg}_2\text{SiO}_4$ ). Compositions that have a steeper spectral index at long wavelengths provide better fits, but the relatively good fit for  $\text{TiO}_2$  (3) (rutile; second lowest  $\chi^2$  in Fig. 13) is an artifact of an unphysically steep extrapolation ( $\lambda^{-3.5}$ ) of the measured optical constants which are not published for  $\lambda \geq 70 \mu\text{m}$ . For the Si II spectrum, any models that are within a factor of 4 of the minimum  $\chi^2$  are deemed acceptable. This includes most dust compositions, and only excludes compositions that have strong features near  $\sim 40 \mu\text{m}$  that would have exceeded the upper limits provided by the *Spitzer* IRS data.

## 5. DISCUSSION

### 5.1. Dust Compositions

The identifications of possible dust compositions in the different environments in Cas A are summarized in Table 4. A single dust composition can never provide a good fit to the observed spectra, except for the Si II spectrum which has only upper limits at  $< 70 \mu\text{m}$ . In general, 2 compositions are sufficient to get acceptable fits to the spectra. The Ar II and Ar III spectra are the only ones that show significant (though small) benefit for the addition of a third composition. Among the 7 characteristic dust spectra examined, the results can be grouped into 3 different families of dust.

The first family is found in association with the Ar II and Ar III emitting ejecta, which are distributed widely across the SNR. This family consists of the Mg silicate with the lowest Mg/Si ratio in combination with one or more other compositions that have featureless spectra. The  $\text{Mg}_{0.7}\text{SiO}_{2.7}$  is a good fit to the 9 and 21  $\mu\text{m}$  peaks in the observed spectrum, but only if a featureless dust composition is also present to reduce the apparent strength of these features. However, the Ar dust spectra also contain a weaker 12  $\mu\text{m}$  feature which is not accounted for by any Mg silicate. Nonstoichiometric spinel with low Mg/Al ratios can provide a feature at approximately the correct wavelength, but only when the dust grains are extremely hot, such that longer wavelength spinel features are relatively faint. A better explanation for the 12  $\mu\text{m}$  feature may be provided by  $\text{SiO}_2$ . The spectrum of  $\text{SiO}_2$  exhibits all three peaks seen in Ar II and Ar III spectra, although they are significantly sharper and slightly bluer than the observed ones, and even in combination with other materials the fits are not very good. However, this is when Mie theory is used to calculate the absorption cross sections assuming small spherical grains. Using a continuous distribution of ellipsoids (CDE) approximation instead broadens and shifts the  $\text{SiO}_2$  features to be a better match as a third component. Jäger et al. (2003) point out that the 12  $\mu\text{m}$   $\text{SiO}_2$  feature disappears in Mg silicates when  $\text{Mg}/\text{Si} > 0.5$ . Therefore, it seems likely that the dust associated with the Ar emission is a mixture of silica and Mg silicate (with  $\text{Mg}/\text{Si} \lesssim 0.5$ ) in combination with a separate featureless dust component. SiC can also provide the 12  $\mu\text{m}$  feature, but again only if CDE calculations are applied to this component. If SiC is present, this would be the only direct evidence of carbon-bearing dust. Table 5 lists the possible origins for the 12  $\mu\text{m}$  feature of the Ar dust.

The strong 21  $\mu\text{m}$  peak in this family has been the hallmark of Cas A IR spectra since it was first observed using the Kuiper Airborne Observatory (KAO) and the *Infrared Space Observatory (ISO)*. On the basis of those data, the peak was suggested to arise from Mg protosilicate (Arendt et al. 1999). Subsequent analysis by Douvion et al. (2001) modeled an *ISO* spectrum as  $\text{MgSiO}_3$ ,  $\text{SiO}_2$  and  $\text{Al}_2\text{O}_3$  with the weak 12  $\mu\text{m}$  feature largely produced by the  $\text{Al}_2\text{O}_3$  as proposed for the feature in “Spectrum 2” of Douvion et al. (1999). Ennis et al. (2006) using *Spitzer* IRS data noted the distinction of several different dust spectra in different parts of Cas A and referred to this as the “Strong 21  $\mu\text{m}$ ” spectrum, and calling it “21  $\mu\text{m}$  peak dust” Rho et al. (2008) modeled it as Mg

protosilicate and  $\text{MgSiO}_3$  with secondary components of  $\text{SiO}_2$ ,  $\text{FeO}$ ,  $\text{FeS}$ ,  $\text{Si}$ , and  $\text{Al}_2\text{O}_3$  and/or  $\text{Fe}$ . Later work indicated that the  $21 \mu\text{m}$  feature may be fit primarily by  $\text{SiO}_2$  grains if CDE calculations rather than spherical grain approximations are used (Rho et al. 2009).

The second dust family is associated with the Ne II emission, which is especially prominent in two opposing “Ne crescents” (Ennis et al. 2006; Smith et al. 2009) in the N and S parts of the SNR. These morphological features are evident in the derived spatial distribution of the Ne II dust shown in Figure 4. This dust has a very smooth spectrum that does not suggest any silicate material. The best fits to the spectrum are found with  $\text{Al}_2\text{O}_3$  in combination with other featureless dust. Featureless dust alone can provide moderately good fits, but a broad asymmetric feature in the  $10 - 20 \mu\text{m}$  portion of the  $\text{Al}_2\text{O}_3$  absorption cross section seems to match the observed spectrum especially well. Alternately, nonstoichiometric spinel can provide the needed emission at  $10 - 20 \mu\text{m}$ , although the spinel absorption efficiency has more detailed substructure that is not evident in the observed spectrum.

This second family corresponds to the “weak  $21 \mu\text{m}$ ” components noted by (Ennis et al. 2006) and Rho et al. (2008), which they also associate with relatively strong Ne emission. However, the fact that they see even a weak  $21 \mu\text{m}$  peak in their spectrum suggests that it is a mixture of what we identify as very distinct Ar and Ne dust families. As in our fitting, (Rho et al. 2008) fit this spectrum with hot and cool featureless dust (C glass) and with an intermediate temperature  $\text{Al}_2\text{O}_3$  components. They included other components to add the weak  $21 \mu\text{m}$  peak that appears in their spectrum. Douvion et al. (1999) had also noted an anti-correlation between the  $9 \mu\text{m}$  silicate emission and Ne II and Ne III emission.

The third dust family is associated with the X-ray Fe emission and the South Spot. This family also seems to match the dust associated with the radio emission, which is expected to be dust that has been swept up from the interstellar or circumstellar medium by the forward shock. The primary component in this family is one of the Mg silicates with high Mg/Si ratios or MgFe silicate:  $\text{Mg}_2\text{SiO}_4$ ,  $\text{Mg}_{2.4}\text{SiO}_{4.4}$ ,  $\text{MgFeSiO}_4$ . Other Mg silicates with  $\text{Mg/Si} \geq 1$  can provide acceptable fits, but the silicates with lower ratios that were needed for the Ar dust are not suitable here because of the changing placement and shape of the  $9$  and  $21 \mu\text{m}$  features.

This dust family is matched by the “Broad” component identified by Ennis et al. (2006) and the “Featureless” component modeled by Rho et al. (2008). In both cases this component is *not* associated with Ar or Ne emission lines, just as we also find. Rho et al. (2008) modeled this component as  $\text{MgSiO}_3$ ,  $\text{FeS}$ , and  $\text{Si}$  combined with  $\text{Al}_2\text{O}_3$ ,  $\text{Mg}_2\text{SiO}_4$  and/or  $\text{Fe}$ . Using  $5-17 \mu\text{m}$  ISO data, Douvion et al. (1999) extracted a spectrum (“Spectrum 3”) from a region that should match our Radio spectrum. Despite the limited wavelength coverage, they also found that the spectrum could be fit with astronomical silicate (Draine & Lee 1984) at  $T \sim 105 \text{ K}$ , as we confirm (in Fig. 19).

The Si II dust has no significant emission across the  $5-40 \mu\text{m}$  wavelength range of the IRS. The three *Herschel* PACS measurements at  $70$ ,  $100$ , and  $160$  are insufficient to constrain the composition

of the associated dust. The Si II dust may belong to one of the above families, or it may be an entirely different composition.

## 5.2. Dust Masses

The modeled dust temperatures and compositions allow the determination of the dust mass in each of the components. The dust mass,  $M_d$ , is calculated as:

$$M_d = \frac{D^2 S_\nu(\lambda)}{\kappa_\nu(\lambda) B_\nu(\lambda, T_d)} \quad (4)$$

where  $D = 3.4$  kpc is the distance to Cas A (Reed et al. 1995),  $S_\nu(\lambda)$  is the total flux density of the component in question,  $\kappa_\nu(\lambda)$  is the mass absorption coefficient appropriate for the derived composition of the dust, and  $B_\nu(\lambda, T_d)$  is the Planck function evaluated at the derived temperature. For each of the models fit to the characteristic spectra, the total mass was calculated by summing Eq. 4 over all temperature components of each of the compositions used in the fit. Generally the total dust mass is dominated by a warm component (60 - 130K) that also produces the bulk of the luminosity. However the X-ray Fe spectrum is an exception where an additional cold component dominates the mass, because the *Herschel* PACS data at 70–160  $\mu\text{m}$  are elevated relative to the shorter wavelength emission. The composition of this cold component is uncertain because absorption efficiencies are smooth and the spectral resolution is poor at the long wavelengths. This situation is worse for the Si II dust which is only detected at  $\geq 70$   $\mu\text{m}$ . Its temperature is relatively well constrained, but its composition, and therefore its mass, is not. If the dust is composed of Mg silicates, then the total mass of the Si II dust is  $\lesssim 0.1 M_\odot$ , but this value can be much lower if other compositions are appropriate. Much higher masses are ruled out by the expected nucleosynthetic yields of various elements, and would imply very high condensation efficiencies given that the mass of the unshocked gas is only  $\sim 0.4 M_\odot$  (DeLaney et al. 2014).

The derived dust masses averaged over all models that fit within a factor of 2 of the minimum  $\chi^2$  and are dominated by Mg silicates (or  $\text{Al}_2\text{O}_3$  for the Ne II spectrum) are listed in Table 4. Figure 21 plots the total dust mass for *all* 2–component models of the Ar II dust spectrum as a function of  $\chi^2$  with color coding to indicate compositions and temperatures. The “good” models are within a factor of 2 of the minimum  $\chi^2$  (to the left of the dashed line). The figure shows that although there are correlations between composition and temperatures, the derived mass is more strongly dependent on the composition than the temperature.

The total mass of warm and hot dust for all components that contribute to the  $< 35$   $\mu\text{m}$  spectrum is found to be  $0.04 \pm 0.01 M_\odot$  (see Table 3). This is consistent with other measurements from *IRAS* (Braun 1987; Arendt 1989; Saken et al. 1992) and other analysis of the *Spitzer* IRS data (Rho et al. 2008) because the mid-IR (12–100  $\mu\text{m}$ ) flux density  $S_\nu(\lambda)$  remains basically the unchanged since the *IRAS* measurements. This is the primary observable factor in determining the mass. When corrected for the same distance, previously published mass estimates contain modest

differences (factors of  $\sim 2$ ) due to different assumptions of the mass absorption coefficients,  $\kappa_\nu(\lambda)$ , and dust temperature,  $T_d$ . *ISO*, *Akari*, BLAST, and *Herschel* have revealed an additional cool dust component in Cas A which contains  $\sim 0.08 M_\odot$  of dust (e.g. Tuffs et al. 1999, 2005; Sibthorpe et al. 2010; Barlow et al. 2010). This cool component is what we associated with the Si II. Our mass estimate of this component is consistent, but is very uncertain due to the unknown composition of the dust, and the difficulty in distinguishing the SNR dust from the heavy confusion of the line of sight ISM at these wavelengths.

## 6. SUMMARY

We have decomposed the spatially resolved IR continuum spectra of dust in the Cas A SNR into contributions from distinct regions of the remnant, comprising: shocked circumstellar and interstellar medium swept up by the forward shock; hot X-ray emitting gas and cooler, denser fine-structure IR line emitting regions that result when the SN ejecta passes through the reverse shock; and unshocked regions of the ejecta that have not yet reached the reverse shock. We then calculated the composition and mass of the dust associated with each region of the ejecta. The methodology and results of our paper can be summarized as follows:

- We started by identifying a set of *spatial templates* to represent various IR emitting regions of Cas A. These were defined by the fine structure IR lines from Ar II, Ar III, Ne II, and Si II, by the X-ray (Fe line), and by the radio synchrotron emission. The spatial templates used for the decomposition are shown in Figure 1.
- We then identified spatially distinct *zones*, shown in Figure 2, in which a given template emission was dominant. We extracted the *characteristic spectra* of the dust in each zone using the procedure described in Section 3. The resulting IR spectra were assumed to represent the different spatial templates, and are presented in Figure 3. Figure 4 shows the derived *spatial distribution* of the dust associated with each of the spectral templates.
- We compiled an extensive list of dust compositions with measured optical constants to calculate their possible contribution to the IR emission from each spatial templates. The dust species fall into 8 broad categories defined by similarity of chemical and/or optical properties: silicates, protosilicates, silica, silicon carbide, carbon and metallic iron, aluminum oxides, oxides, and sulfides. The dust compositions used in the analysis are listed in Table 2.
- We fit each characteristic spectrum with all possible combinations of 2 distinct dust species (1711 combinations), allowing each dust species to emit at a range of temperatures. Figures 7–13 depict the  $\chi^2$  values to give an overview of which compositions can provide good fits to the characteristic spectra. Figures 14–20 provide examples of how well the spectra can be fit using 2 (and sometimes 3) dust species.

- The primary dust composition could be readily identified in spectra that have strong IR dust features. The Ar II and Ar III characteristic spectra exhibited strong features at  $\sim 9$  and  $21 \mu\text{m}$ . Magnesium silicates, characterized by a Mg/Si ratio of 0.7 (i.e.  $\text{Mg}_{0.7}\text{SiO}_{2.7}$ ) provided the best fit to the spectra of these regions. The Ne II spectrum was best fit with  $\text{Al}_2\text{O}_3$  dust, and the X-ray Fe spectrum, which exhibit peaks at  $\sim 10$  and  $20 \mu\text{m}$  was best fit with silicates having a higher Mg/Si ratio of 2.4 (i.e.  $\text{Mg}_{2.4}\text{SiO}_{4.4}$ ). A region called the South Spot had similar composition. The dust composition associated with the spectrum of the radio synchrotron emitting region behind the SNR’s forward shock was consistent with that expected for typical interstellar dust. The IR spectrum from the Si II emitting region arises from a cold dust component that is only seen at long wavelengths. Since very few dust compositions have distinguishing features at these wavelengths, and because these broad band data at long wavelengths provide little detail on the spectrum, the composition of this cold dust could not be determined.
- Secondary dust components are needed to improve the fit for most spectra, but these components are not uniquely identified. Table 3 lists the primary dust composition for each spectrum, and all possible secondary dust species that they need to be paired with. The secondary dust species generally have a featureless dust spectrum.
- A minimal number of only 4 dust species:  $\text{Mg}_{0.7}\text{SiO}_{2.7}$ ,  $\text{Mg}_{2.4}\text{SiO}_{4.4}$ ,  $\text{Al}_2\text{O}_3$ , and amorphous carbon, would be sufficient to fit the entire spectrum of Cas A. These compositions suggest that the seed dust particles that formed the more complex species are MgO,  $\text{SiO}_2$ ,  $\text{Al}_2\text{O}_3$ , and carbon.
- The total mass of dust is about  $0.04 M_\odot$  in the shocked CSM/ISM and ejecta regions, and  $\lesssim 0.1 M_\odot$  in the unshocked ejecta characterized by the Si II emission. This dust mass is similar to that derived by Rho et al. (2008) from the *Spitzer* data, and the  $\sim 0.08 M_\odot$  derived for dust in the cold unshocked ejecta derived from the *Herschel*, BLAST, and *Akari* data (Barlow et al. 2010; Sibthorpe et al. 2010).

This work is based on observations made with the *Spitzer Space Telescope*, which is operated by the Jet Propulsion Laboratory, California Institute of Technology under a contract with NASA. Support for this work was provided by NASA Program NNH09ZDA001N-ADP-0032. This research made use of Tiny Tim/*Spitzer*, developed by John Krist for the Spitzer Science Center. The Center is managed by the California Institute of Technology under a contract with NASA This research has made use of NASA’s Astrophysics Data System Bibliographic Services. We thank T. Kozasa for providing digitized (and extrapolated and interpolated) versions of the optical constants for several dust species as noted in Table 3. We also thank the referee for constructive comments on the manuscript.

*Facilities:* Spitzer, Herschel, CXO, VLA



### A. Selection of Spatial Templates

A set of spatial templates are needed to distinguish different physical environments within the SNR. We want to be able to distinguish swept-up ISM or CSM dust from ejecta dust, to probe the nature of ejecta dust created in different nucleosynthetic layers of the SN, and to investigate ejecta dust in preshock and postshock regions having different gas temperatures and densities. The primary source for templates are the line emission maps that are generated by subtracting the continuum cube from the full data cube, and then integrating over the  $[-6000,+8000]$  km s<sup>-1</sup> velocity range for each of the emission lines in the IRS spectrum (see Table 1). Most of these lines are associated with the fast-moving knots of ejecta. These knots tend to be O-rich, but there are some variations in composition that tend to be correlated with spatial and kinematic differences. Because of the large range in velocity in the Cas A ejecta, closely spaced [O IV] 25.89  $\mu$ m and [Fe II] 25.99  $\mu$ m lines would be confused in the low resolution spectra. However, Isensee et al. (2010, 2012) report that high resolution spectra show that Cas A’s 26  $\mu$ m line is entirely produced by [O IV] without any contribution from [Fe II].

Several other spatial templates were also tested. These are intended to trace the presence of dust in a wider range of environments than the relatively cool and dense line-emitting knots:

- (1) A radio template was derived from 6 cm VLA image of Cas A (DeLaney 2004). The region of the forward shock is traced more clearly in the radio than at most other wavelengths, and the bright radio knots in the reverse shock region are a different population than line-emitting ejecta knots.
- (2) and (3) X-ray Fe and Si templates were derived from *Chandra* observations (Hwang et al. 2004), integrated over the widths of the 6.4 keV Fe and 1.7 keV Si K  $\alpha$  lines. The X-ray continuum is included in these integrations. These templates trace ejecta in regions of lower density and much higher temperature. These regions include the bulk of the mass of the ejecta of the SN.
- (4) The IRAC 4.5  $\mu$ m image lies outside the range of the IRS spectral coverage and contains both a synchrotron component and a probable line emission component. The synchrotron emission was subtracted using a scaled version of the IRAC 3.6  $\mu$ m image which is dominated by synchrotron emission and has only weak line emission. However, this over-subtracts stellar sources in the image. Thus regions where negative values resulted were replaced by nearby background values.
- (5) The IRAC 8  $\mu$ m image is dominated by the [Ar II] 6.99  $\mu$ m emission, but was considered as a potentially cleaner map of this line than the IRS line maps. The background ISM emission at 8  $\mu$ m was removed by subtracting a scaled version of the 5.8  $\mu$ m IRAC image, where the SNR emission is relatively weaker. As with the 4.5  $\mu$ m template, the over-subtracted stellar sources were replaced by the local background levels.

Each of these templates is convolved and reprojected to match the IRS continuum data cube.

This full set of templates would be expected to contain some degeneracies, where different lines (especially from the same species or element) would be tracing the same physical component of the SNR. To select a useful subset of the possible templates, we calculated the linear correlation coefficient for each pair of templates. These are listed in Table 1. The table shows which templates

are well-correlated with others. Based on these correlations we sorted the templates in to similar groups and selected one template to represent each group. Images of the selected templates are shown in Figure 1.

There are several points of interest in the correlations listed in Table 1. Even though the [Ar II] and [Ar III] emission are very well correlated (as expected), we chose to keep both these templates in order to monitor for changes in the dust that might be related to the ionization state of the gas. It was not expected that highly ionized species such as [S IV] would correlate so well with [Ar II]. This correlation may become significantly weaker if higher spatial resolution data were available. Correlations involving the [Fe II] line are weaker than most due to the low signal to noise ratio of this line. The [Ne V] line is also relatively weak, yet surprisingly it correlates better with the [Ar II] group than the [Ne II] and [Ne III] lines. Despite an absence of Ne lines in the band, the 4.5  $\mu\text{m}$  IRAC  $\mu\text{m}$  emission is somewhat better correlated with the Ne group templates than the Ar group. In particular, the “Ne crescents” noted by Ennis et al. (2006) are present in the IRAC 4.5  $\mu\text{m}$  image. Although the [S III] 33.48  $\mu\text{m}$  correlates moderately well with the [S III] 18.71  $\mu\text{m}$  line, it does not correlate as well with the other templates of the Ar group. This is an indication of variation in the S III line ratios, which would indicate large scale variations in the density of the ejecta (Smith et al. 2009). The [O IV] 25.89  $\mu\text{m}$  and [S III] 33.48  $\mu\text{m}$  templates are moderately correlated with the both the Si II template and the Ar-like templates. Because the [O IV] and [S III] templates did not have distinct features lacking in these other templates, we did not use either in the analysis. The X-ray Si template is in fact distinct from the X-ray Fe template, but it was not used because initial analysis using only the X-ray Fe template did not indicate the presence of any residual emission that would have been reduced by the addition of an X-ray Si template.

## REFERENCES

- Arendt, R. G. 1989, *ApJS*, 70, 181
- Arendt, R. G., Dwek, E., & Moseley, S. H. 1999, *ApJ*, 521, 234
- Barlow, M. J., Krause, O., Swinyard, B. M., et al. 2010, *A&A*, 518, L138
- Begemann, B., Dorschner, J., Henning, T., & Mutschke, H. 1996, *ApJ*, 464, L195
- Begemann, B., Dorschner, J., Henning, T., et al. 1997, *ApJ*, 476, 199
- Begemann, B., Dorschner, J., Henning, T., Mutschke, H., & Thamm, E. 1994, *ApJ*, 423, L71
- Bohren, C. F., & Huffman, D. R. 1983, *Absorption and Scattering of Light by Small Particles* (New York: Wiley)
- Braatz, A., Ott, U., Henning, T., Jäger, C., & Jeschke, G. 2000, *Meteoritics and Planetary Science*, 35, 75

- Brandt, T. D., & Draine, B. T. 2012, *ApJ*, 744, 129
- Braun, R. 1987, *A&A*, 171, 233
- Cherchneff, I. 2012, *A&A*, 545, A12
- DeLaney, T., Kassim, N. E., Rudnick, L., & Perley, R. A. 2014, *ApJ*, arXiv:1403.0032
- DeLaney, T. A. 2004, PhD thesis, University of Minnesota
- Dorschner, J., Begemann, B., Henning, T., Jaeger, C., & Mutschke, H. 1995, *A&A*, 300, 503
- Dorschner, J., Friedemann, C., Guertler, J., & Duley, W. W. 1980, *Ap&SS*, 68, 159
- Douvion, T., Lagage, P. O., & Cesarsky, C. J. 1999, *A&A*, 352, L111
- Douvion, T., Lagage, P. O., & Pantin, E. 2001, *A&A*, 369, 589
- Draine, B. T., & Lee, H. M. 1984, *ApJ*, 285, 89
- Draine, B. T., & Li, A. 2007, *ApJ*, 657, 810
- Dwek, E., & Cherchneff, I. 2011, *ApJ*, 727, 63
- Edoh, O. 1983, PhD thesis, The University of Arizona
- Edwards, D. F. 1985, *Handbook of Optical Constants of Solids*, ed. E. D. Palik (San Diego, CA: Academic Press), 547
- Ennis, J. A., Rudnick, L., Reach, W. T., et al. 2006, *ApJ*, 652, 376
- Fabian, D., Henning, T., Jäger, C., et al. 2001, *A&A*, 378, 228
- Fesen, R. A., Hammell, M. C., Morse, J., et al. 2006, *ApJ*, 645, 283
- Forrest, W. J., Houck, J. R., & McCarthy, J. F. 1981, *ApJ*, 248, 195
- Gordon, K. D., Engelbracht, C. W., Rieke, G. H., et al. 2008, *ApJ*, 682, 336
- Griffin, M. J., Abergel, A., Abreu, A., et al. 2010, *A&A*, 518, L3
- Henning, T., Begemann, B., Mutschke, H., & Dorschner, J. 1995, *A&AS*, 112, 143
- Hony, S., Waters, L. B. F. M., & Tielens, A. G. G. M. 2002, *A&A*, 390, 533
- Hwang, U., Laming, J. M., Badenes, C., et al. 2004, *ApJ*, 615, L117
- Isensee, K., Rudnick, L., DeLaney, T., et al. 2010, *ApJ*, 725, 2059
- Isensee, K., Olmschenk, G., Rudnick, L., et al. 2012, *ApJ*, 757, 126

- Jaeger, C., Mutschke, H., Begemann, B., Dorschner, J., & Henning, T. 1994, *A&A*, 292, 641
- Jäger, C., Dorschner, J., Mutschke, H., Posch, T., & Henning, T. 2003, *A&A*, 408, 193
- Jiang, B. W., Zhang, K., & Li, A. 2005, *ApJ*, 630, L77
- Krause, O., Birkmann, S. M., Usuda, T., et al. 2008, *Science*, 320, 1195
- Li, A., & Draine, B. T. 2001, *ApJ*, 554, 778
- Lynch, D. W., & Hunter, W. R. 1991, *Handbook of Optical Constants of Solids II*, ed. E. D. Palik (San Diego, CA: Academic Press), 341
- Markwardt, C. B. 2009, in *Astronomical Society of the Pacific Conference Series*, Vol. 411, *Astronomical Data Analysis Software and Systems XVIII*, ed. D. A. Bohlender, D. Durand, & P. Dowler, 251
- Mukai, T. 1989, in *Evolution of Interstellar Dust and Related Topics*, ed. A. Bonetti, J. M. Greenberg, & S. Aiello, 397
- Mutschke, H., Andersen, A. C., Jäger, C., Henning, T., & Braatz, A. 2004, *A&A*, 423, 983
- Mutschke, H., Posch, T., Fabian, D., & Dorschner, J. 2002, *A&A*, 392, 1047
- Nozawa, T., Kozasa, T., Tominaga, N., et al. 2010, *ApJ*, 713, 356
- . 2008, *ApJ*, 684, 1343
- Omont, A., Moseley, S. H., Cox, P., et al. 1995, *ApJ*, 454, 819
- Philipp, H. R. 1985, *Handbook of Optical Constants of Solids*, ed. E. D. Palik (San Diego, CA: Academic Press), 749
- Pilbratt, G. L., Riedinger, J. R., Passvogel, T., et al. 2010, *A&A*, 518, L1
- Piller, H. 1985, *Handbook of Optical Constants of Solids*, ed. E. D. Palik (San Diego, CA: Academic Press), 571
- Poglitsch, A., Waelkens, C., Geis, N., et al. 2010, *A&A*, 518, L2
- Posch, T., Kerschbaum, F., Fabian, D., et al. 2003, *ApJS*, 149, 437
- Reed, J. E., Hester, J. J., Fabian, A. C., & Winkler, P. F. 1995, *ApJ*, 440, 706
- Rest, A., Foley, R. J., Sinnott, B., et al. 2011, *ApJ*, 732, 3
- Rho, J., Kozasa, T., Reach, W. T., et al. 2008, *ApJ*, 673, 271
- Rho, J., Reach, W. T., Tappe, A., et al. 2009, in *Astronomical Society of the Pacific Conference Series*, Vol. 414, *Cosmic Dust - Near and Far*, ed. T. Henning, E. Grün, & J. Steinacker, 22

- Rinehart, S. A., Benford, D. J., Cataldo, G., et al. 2011, *Appl. Opt.*, 50, 4115
- Rouleau, F., & Martin, P. G. 1991, *ApJ*, 377, 526
- Saken, J. M., Fesen, R. A., & Shull, J. M. 1992, *ApJS*, 81, 715
- Semenov, D., Henning, T., Helling, C., Ilgner, M., & Sedlmayr, E. 2003, *A&A*, 410, 611
- Sibthorpe, B., Ade, P. A. R., Bock, J. J., et al. 2010, *ApJ*, 719, 1553
- Siebenmorgen, R., Voshchinnikov, N. V., & Bagnulo, S. 2014, *A&A*, 561, A82
- Smith, J. D. T., Rudnick, L., Delaney, T., et al. 2009, *ApJ*, 693, 713
- Tuffs, R. J., Fischera, J., Drury, L. O., et al. 1999, in *ESA Special Publication*, Vol. 427, *The Universe as Seen by ISO*, ed. P. Cox & M. Kessler, 241
- Tuffs, R. J., Popescu, C. C., & Völk, H. J. 2005, in *ESA Special Publication*, Vol. 577, *ESA Special Publication*, ed. A. Wilson, 427–428
- Valiante, R., Schneider, R., Salvadori, S., & Bianchi, S. 2011, *MNRAS*, 416, 1916
- Zeidler, S., Posch, T., Mutschke, H., Richter, H., & Wehrhan, O. 2011, *A&A*, 526, A68
- Zinner, E. 2008, *PASA*, 25, 7
- Zubko, V., Dwek, E., & Arendt, R. G. 2004, *ApJS*, 152, 211

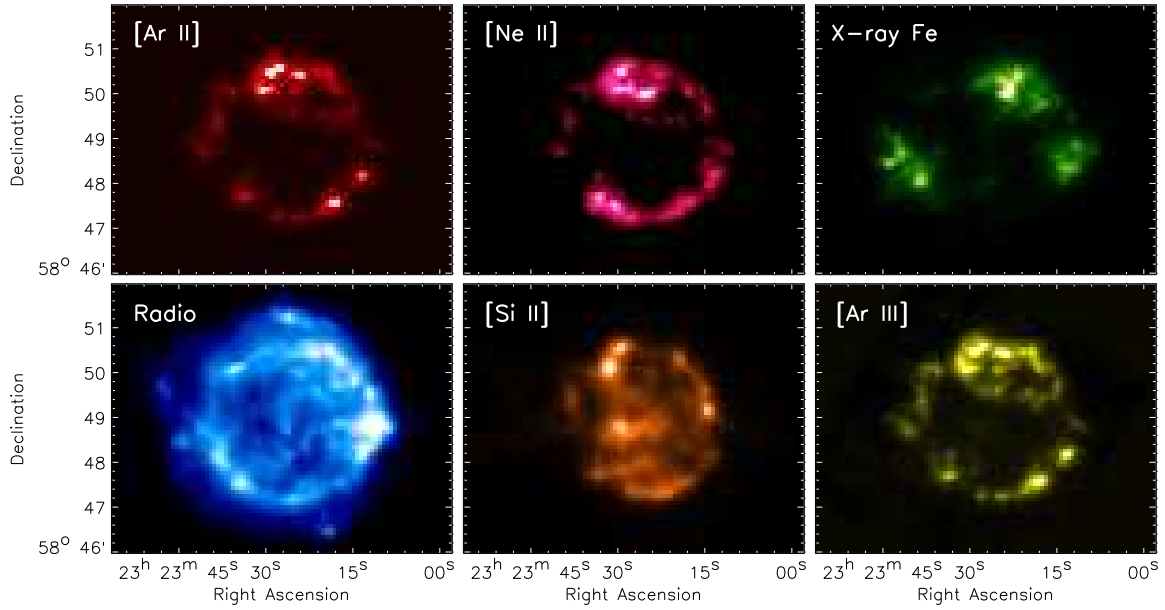


Fig. 1.— Spatial templates used to signify regions that may contain dust distinguished by different composition, origin (ejecta vs. ISM), and/or heating. The [Ar II]  $6.99 \mu\text{m}$ , [Ne II]  $12.81 \mu\text{m}$ , [Si II]  $34.8 \mu\text{m}$ , [Ar III]  $8.99 \mu\text{m}$  lines are derived from the IRS data cube. The X-ray Fe emission is from Hwang et al. (2004) and the VLA 6 cm radio map is from DeLaney (2004).

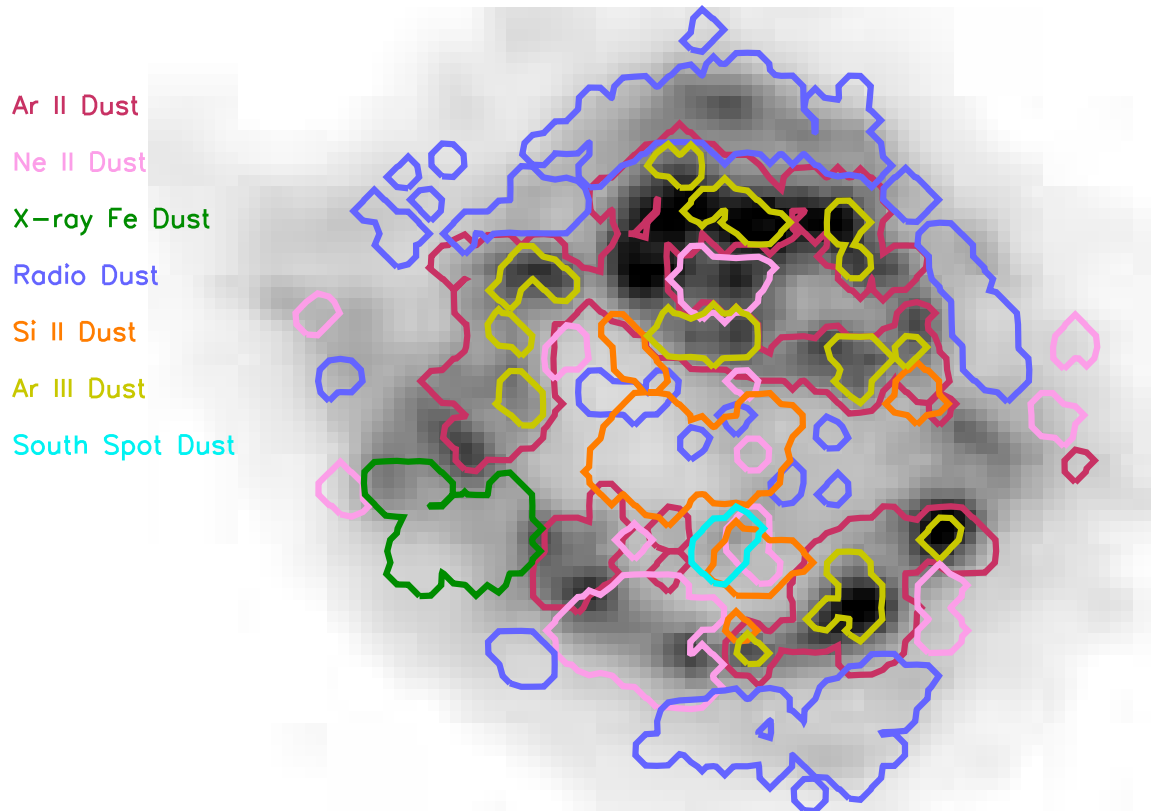


Fig. 2.— Depiction of the zones within which the characteristic spectra of each spatial template were extracted. These zones correspond to the regions where the templates shown in Figure 1 are dominant (apart from the nearly ubiquitous Ar II). The additional “South Spot” zone was identified as the primary region where there is relatively strong continuum emission that is not traced by any of the spatial templates.

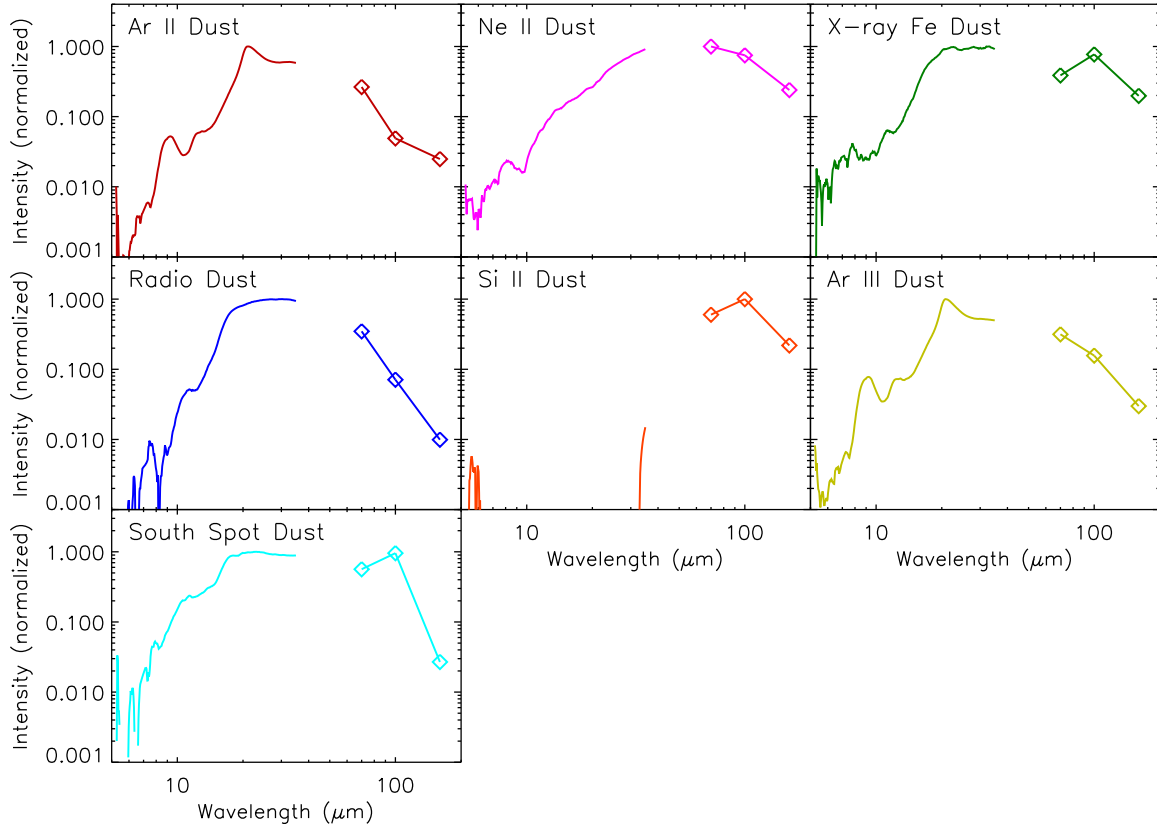


Fig. 3.— The characteristic spectra extracted for each of the spectral zones defined in Figure 2. In each case, the solid line from 5 – 35  $\mu\text{m}$  is the IRS data. The three points at 70, 100, and 160  $\mu\text{m}$  are broadband *Herschel* PACS data. (The Si II dust has no significant emission at  $\leq 35 \mu\text{m}$ ).



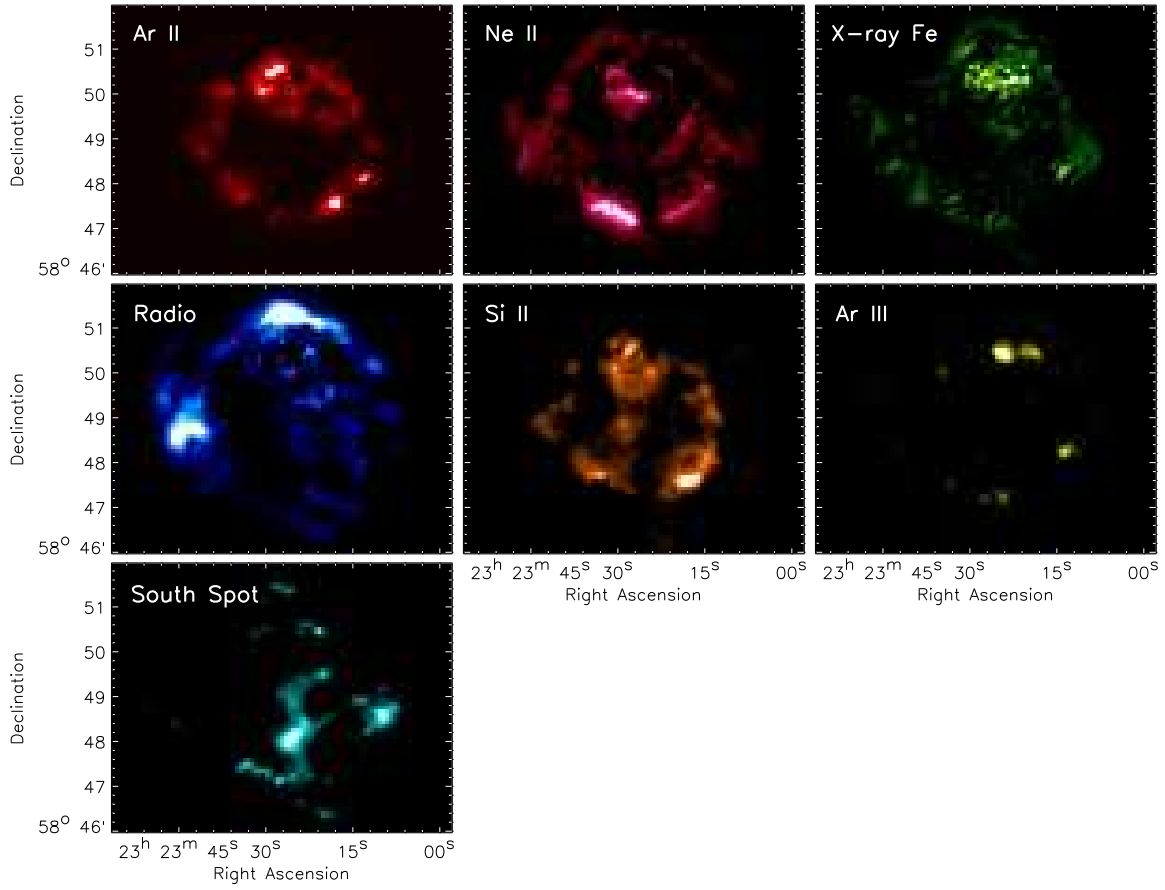


Fig. 4.— Spatial distribution of the dust associated with each of the characteristic spectra shown in Figure 3.

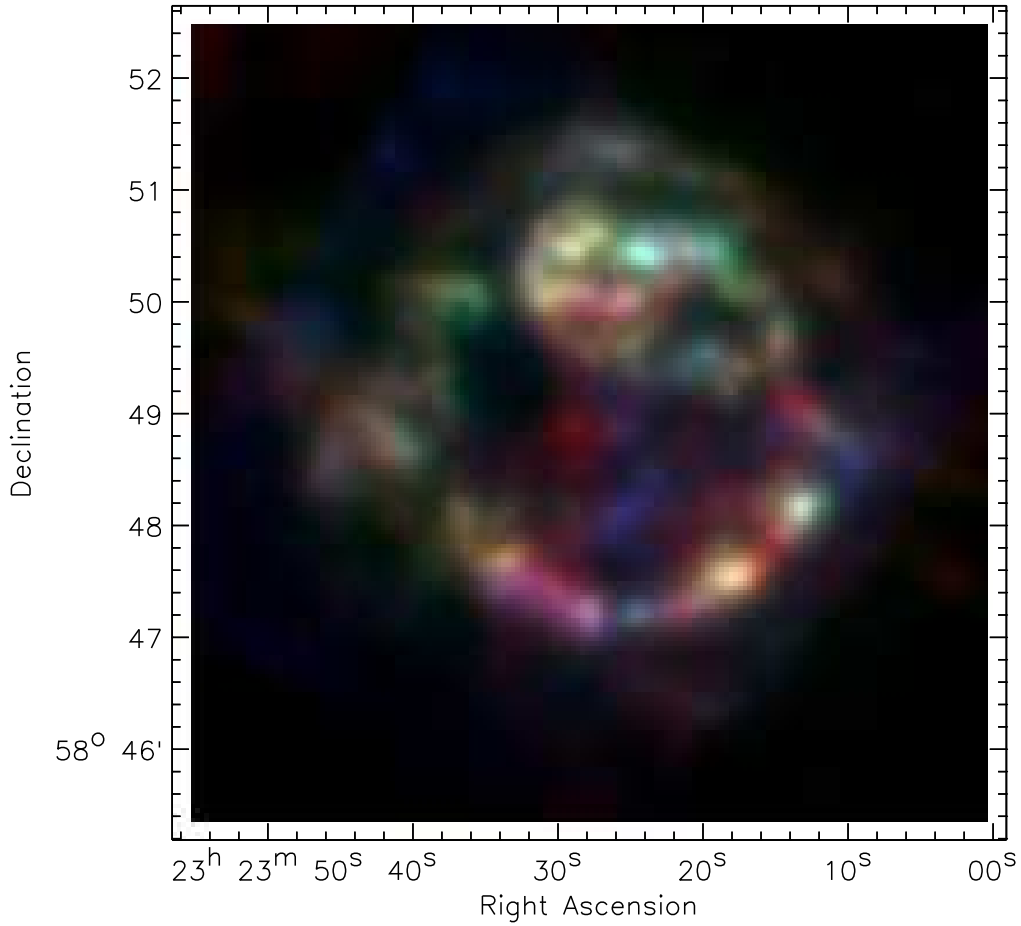


Fig. 5.— This color image of Cas A dust displays continuum emission at 11.8, 20.8, 70  $\mu\text{m}$  in the blue, green, and red channels, respectively. Comparison with Figure 4 shows that these wavelengths provide good illustration of the different dust types: Ar II = green, Ne II = pink, Radio = grey, Si II = red, Ar III = pale cyan, South Spot = purple. (X-ray Fe dust is not clearly distinguished.)

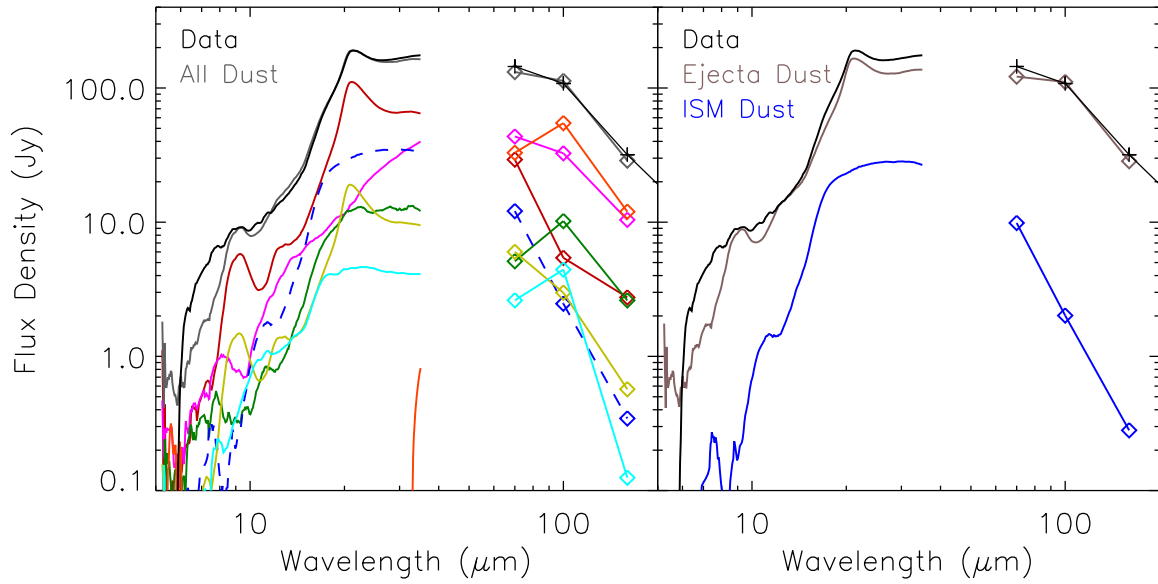


Fig. 6.— (left) Comparison of the relative intensities of each of the spectral types with the total emission of Cas A. The gray line is the sum of all the characteristic spectra. The black line at  $\lambda \leq 35 \mu\text{m}$  is the total of our *Spitzer* IRS spectral cube. The black points at  $\lambda \geq 70 \mu\text{m}$  are the *Herschel* PACS measurements with synchrotron emission and ISM background subtracted (Barlow et al. 2010). (right) Comparison of the total Cas A emission with the sum of all the ejecta dust components and the ISM dust component. The ISM dust component is that associated with the radio emission of the forward shock.

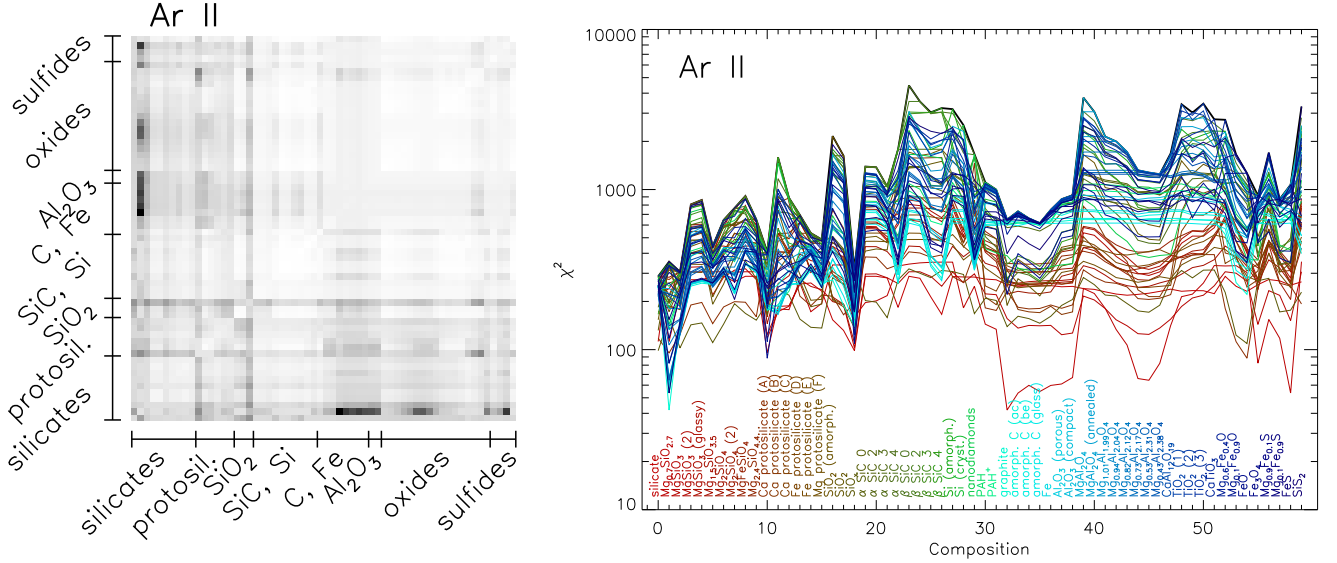


Fig. 7.— (left) A map of  $\chi^2$  for 2-composition models of the Ar II dust spectrum. Darker shading indicates lower values. The map shows that the lowest values of  $\chi^2$  are achieved when one of the silicates (second row from bottom) is paired with the relatively featureless dust such as C, Fe, or  $\text{Al}_2\text{O}_3$ . Good fits are also obtained by pairing this silicate with nonstoichiometric spinels ( $\text{MgAl}_2\text{O}_4$ , i.e. oxides) with low Mg/Al ratios. (right) In this alternate depiction of  $\chi^2$  for 2-composition models, each line plotted shows  $\chi^2$  for a given “primary” dust component (as coded by line/label colors) when paired with each possible “secondary” component (as listed in order along the abscissa). Thus each plotted line corresponds to a row in the matrix shown to the left. Here one can see more specifically that  $40 < \chi^2 < 80$  for  $\text{Mg}_{0.7}\text{SiO}_{2.7}$  when paired with the relatively featureless graphite, amorphous C, Fe,  $\text{Al}_2\text{O}_3$ ,  $\text{Fe}_3\text{O}_4$ , and FeS, or with the nonstoichiometric spinels with low Mg/Al ratios.

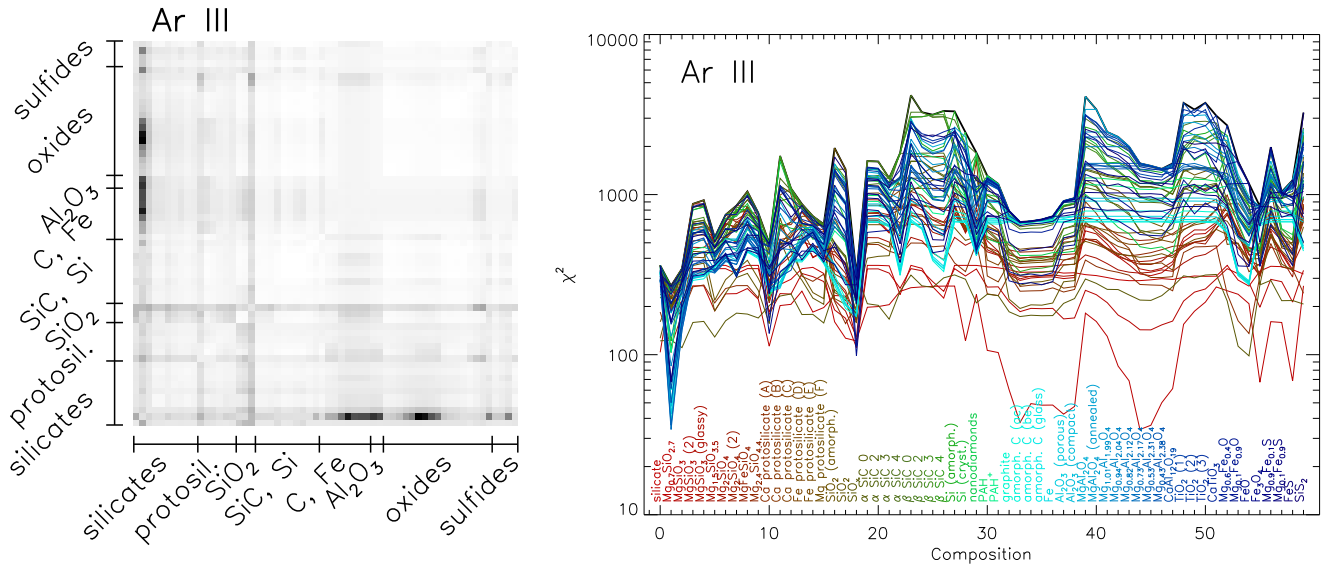


Fig. 8.—  $\chi^2$  as in Fig. 7, but for the Ar III dust spectrum. Because the Ar III dust spectrum is very similar to the Ar II dust spectrum,  $\chi^2$  for each pair of compositions is very similar in both cases.

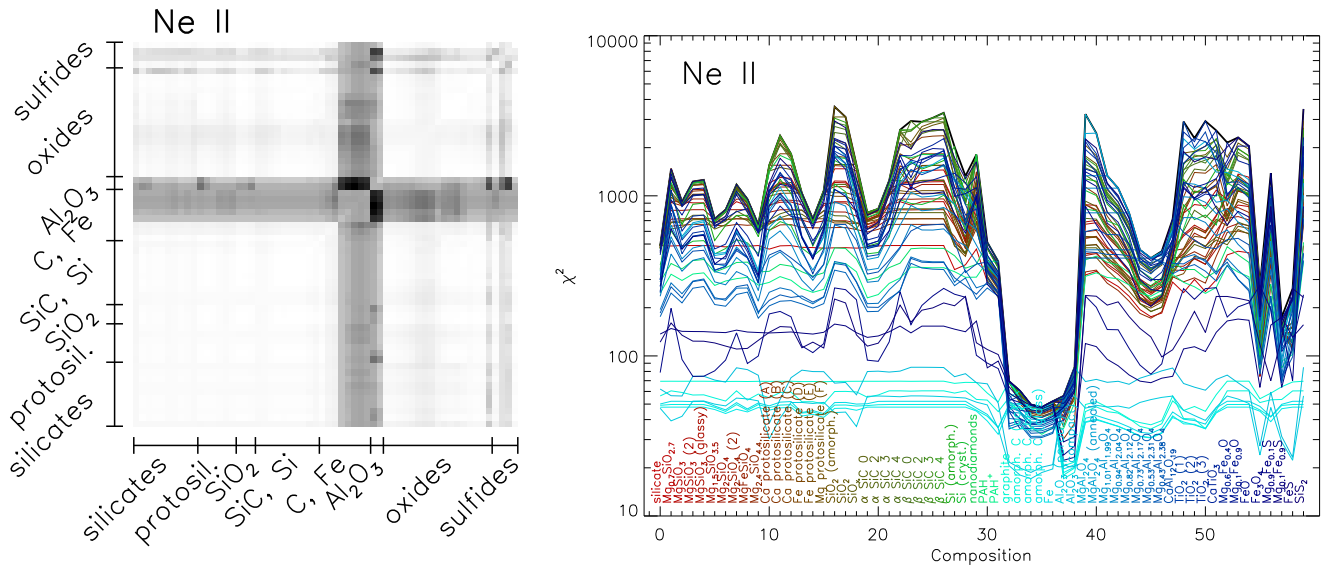


Fig. 9.—  $\chi^2$  as in Fig. 7, but for the Ne II dust spectrum. The best models contain either porous or compact  $\text{Al}_2\text{O}_3$  paired with any of the more featureless dust components.

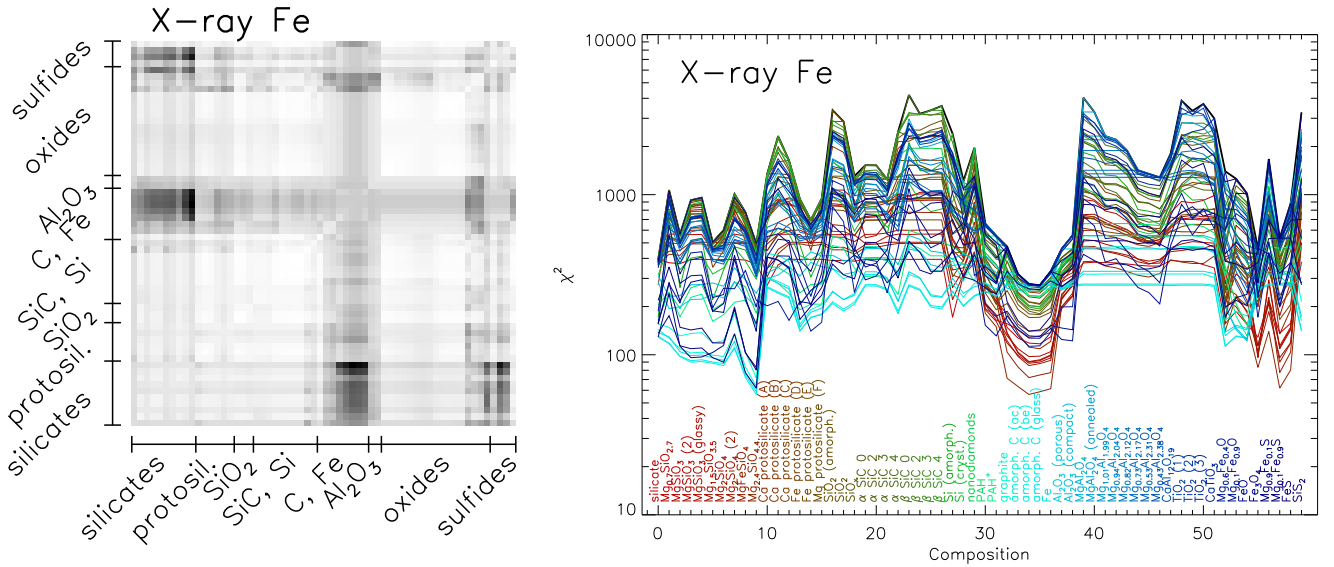


Fig. 10.—  $\chi^2$  as in Fig. 7, but for the X-ray Fe dust spectrum. This spectrum is best fit by silicates with high Mg/Si ratios and paired with the relatively featureless compositions.

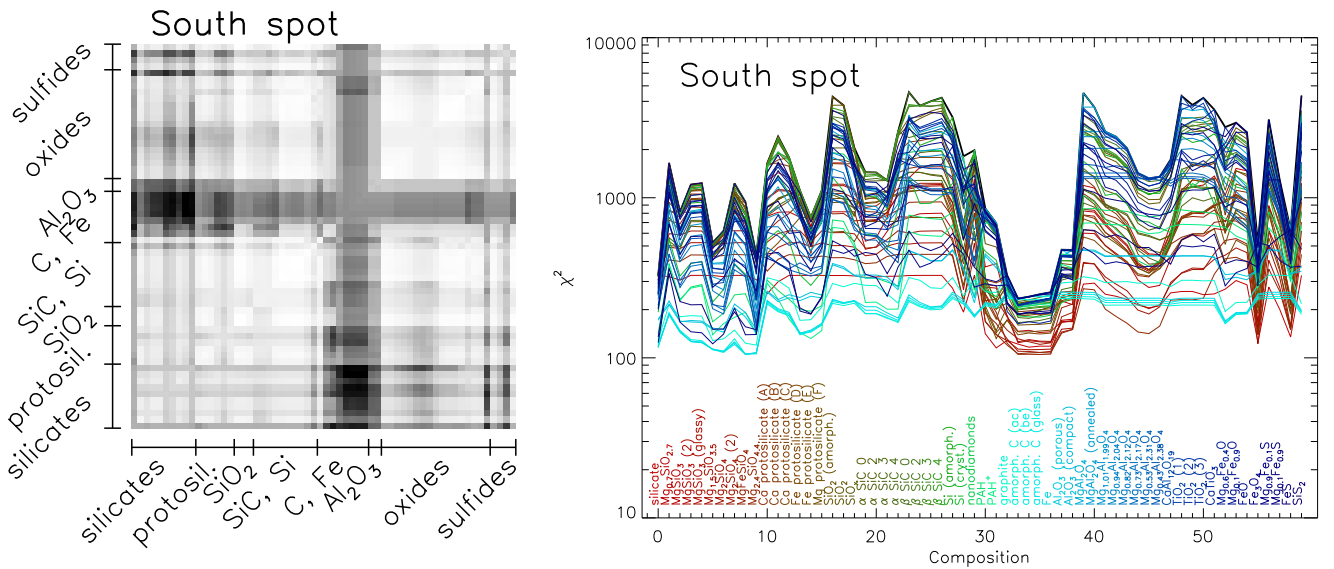


Fig. 11.—  $\chi^2$  as in Fig. 7, but for the South Spot dust spectrum. The results here are very similar to those for the X-ray Fe spectrum, but with somewhat less contrast between the best fits and the more marginal ones.



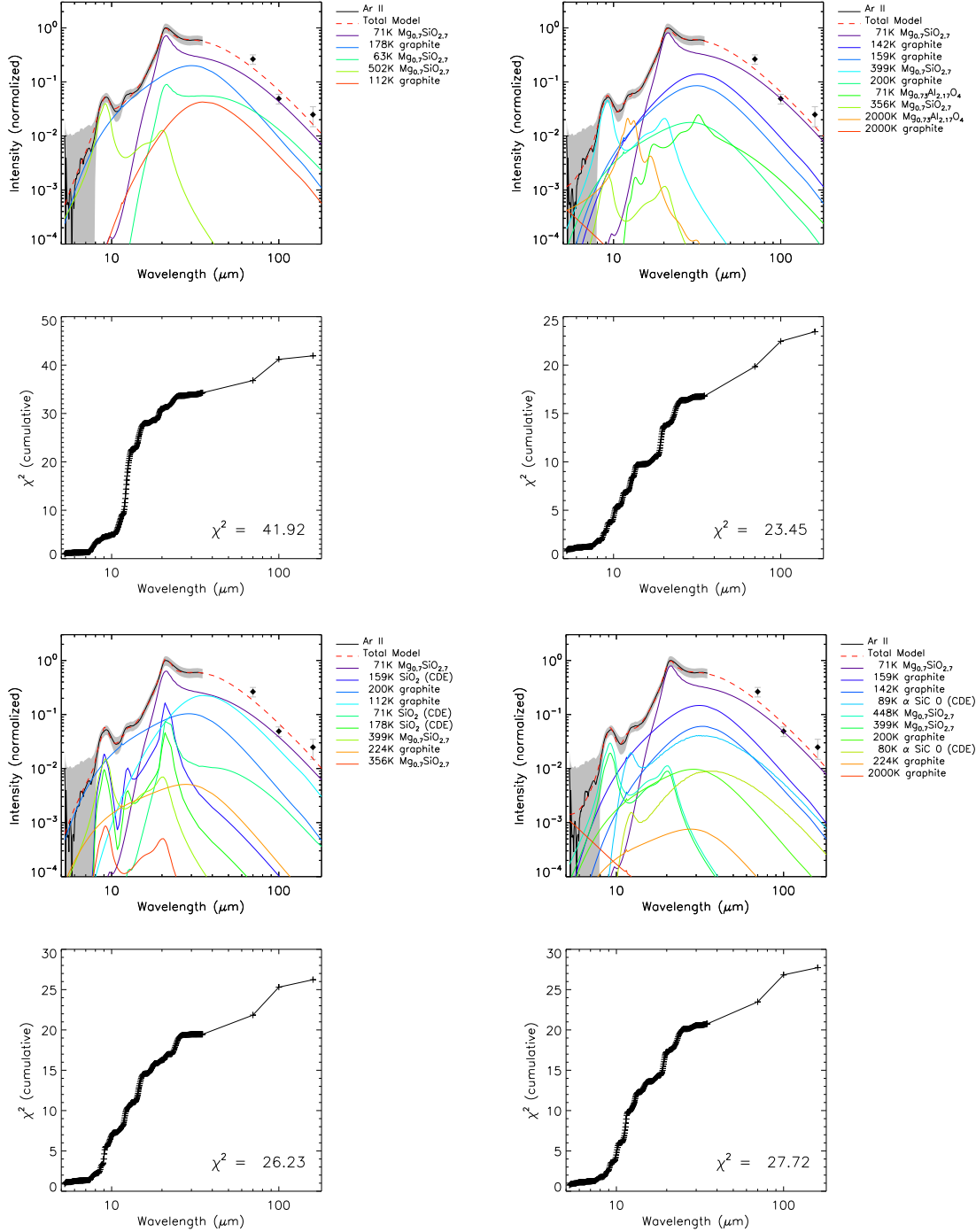


Fig. 14.— (upper left) The best 2-composition fit to the Ar II spectrum includes  $\text{Mg}_{0.7}\text{SiO}_{2.7}$  and a featureless dust composition. Uncertainties of the IRS data are indicated by the gray band. The lower panel shows how  $\chi^2$  accumulates as a function of wavelength. (upper right) The best 3-component fit to the spectrum is a good match to all of the features at 9, 12 and 21  $\mu\text{m}$ . However, the 12  $\mu\text{m}$  feature is provided by implausibly hot nonstoichiometric spinel. (lower left) A very good 3-component fit can also be obtained with  $\text{SiO}_2$  as the third component, if its mass absorption coefficient is calculated via CDE rather than Mie theory.  $\text{SiO}_2$  has features at each of the observed peaks. (lower right) Another very good fit can be obtained with SiC as the third component, again if its mass absorption coefficient is calculated via CDE rather than Mie theory. SiC contributes only at 12  $\mu\text{m}$ , but may also provide a partial match of the 21  $\mu\text{m}$  feature (Jiang et al. 2005).



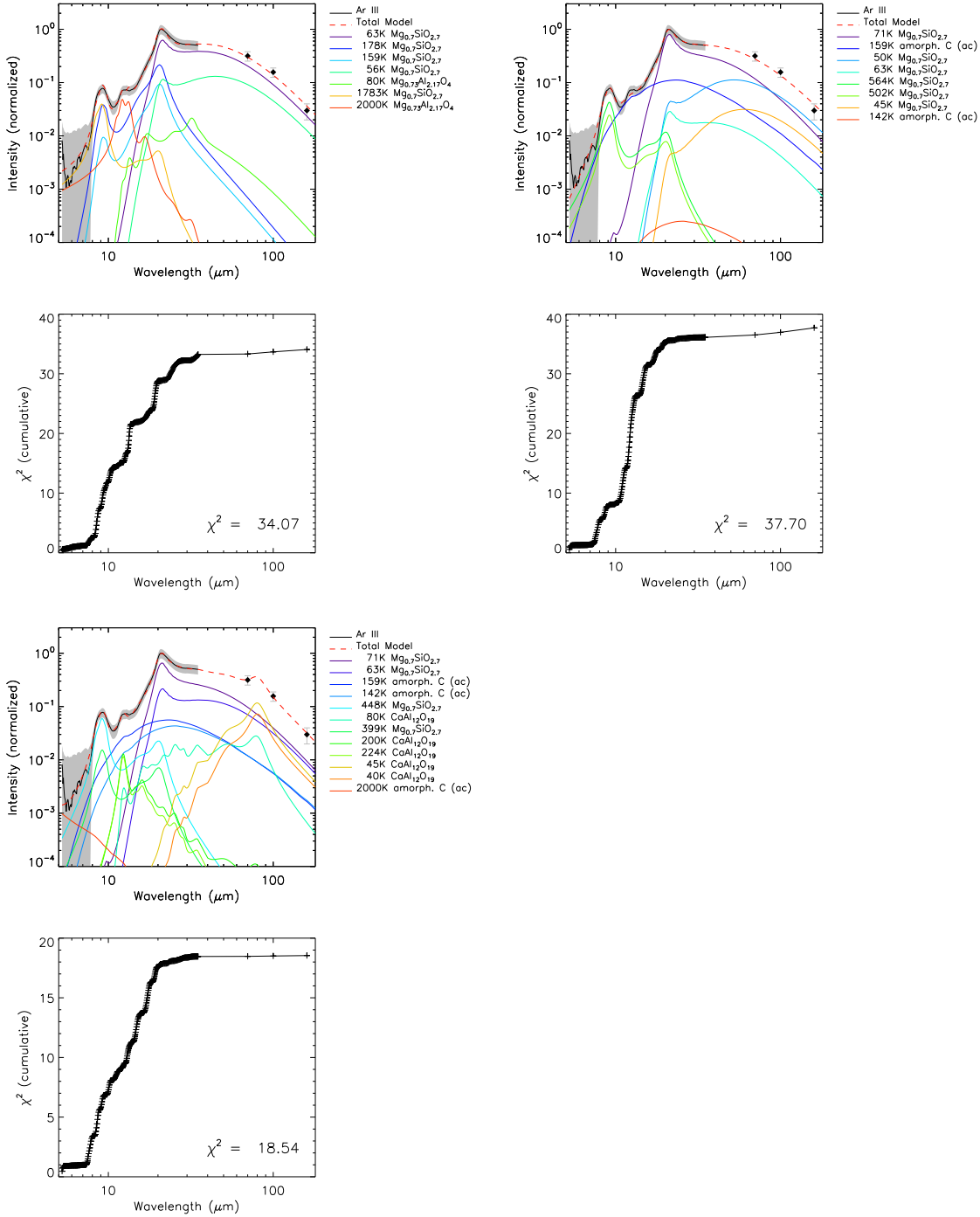


Fig. 15.— (upper left) The best 2-composition fit to the Ar III spectrum makes use of the 12  $\mu\text{m}$  feature of nonstoichiometric spinel. (upper right) Alternate 2-component fits to the spectrum using featureless compositions (e.g. amorphous C) fit nearly as well, but do not match the 12  $\mu\text{m}$  peak. (lower left) The best 3-component fit uses  $CaAl_{12}O_{19}$  (hibonite) to fit the 12  $\mu\text{m}$  peak.

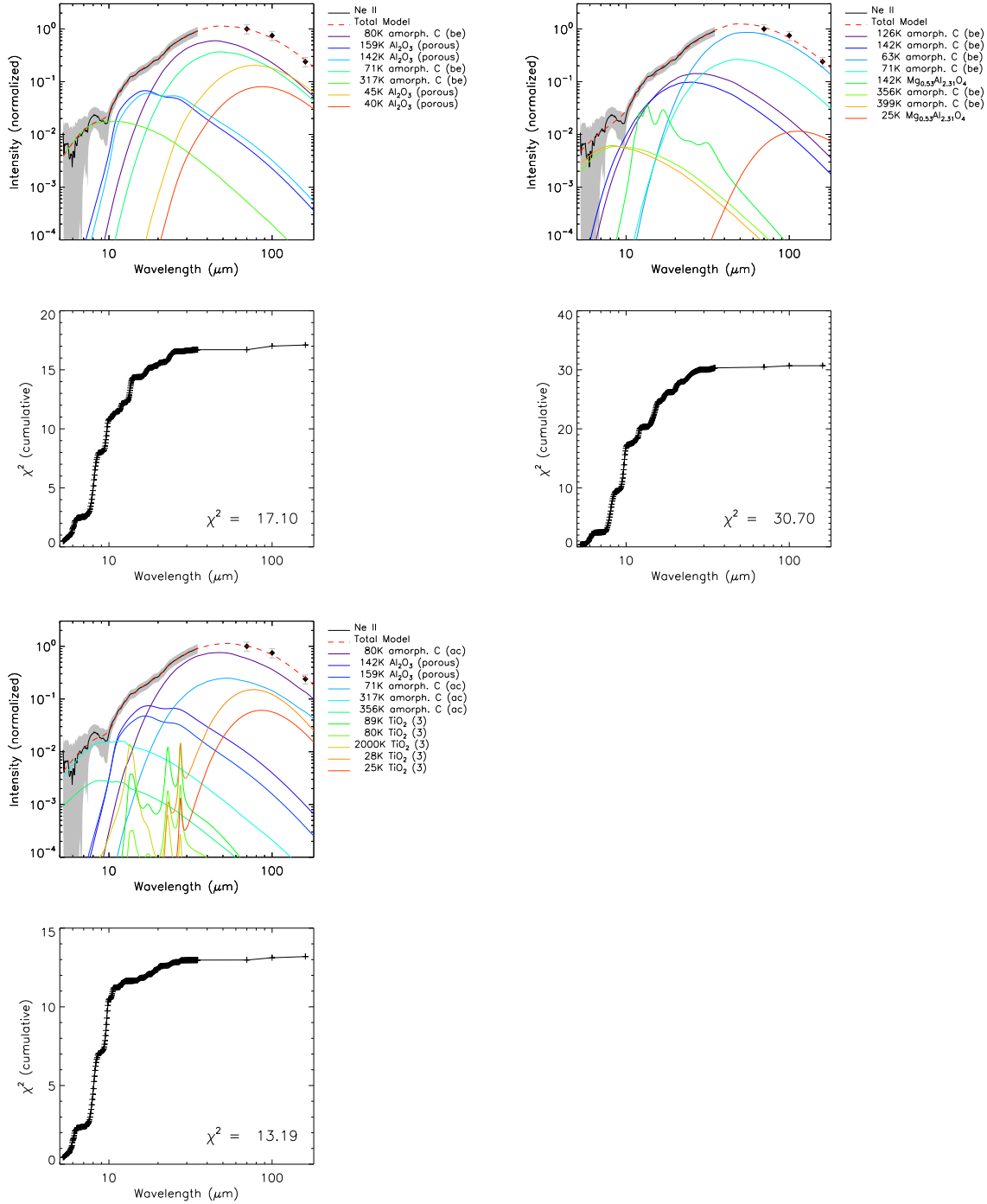


Fig. 16.— (upper left) The best 2-component fits to the Ne II spectrum use Al<sub>2</sub>O<sub>3</sub> in combination with a more featureless component. None of the silicates are a good match for this very smooth spectrum. (upper right) An alternate 2-component fit to the spectrum can be found using non-stoichiometric spinel instead of Al<sub>2</sub>O<sub>3</sub>. (lower left) The best 3-component fit adds TiO<sub>2</sub>, but the improvement in the fit is very small and does not justify the addition of the third composition.

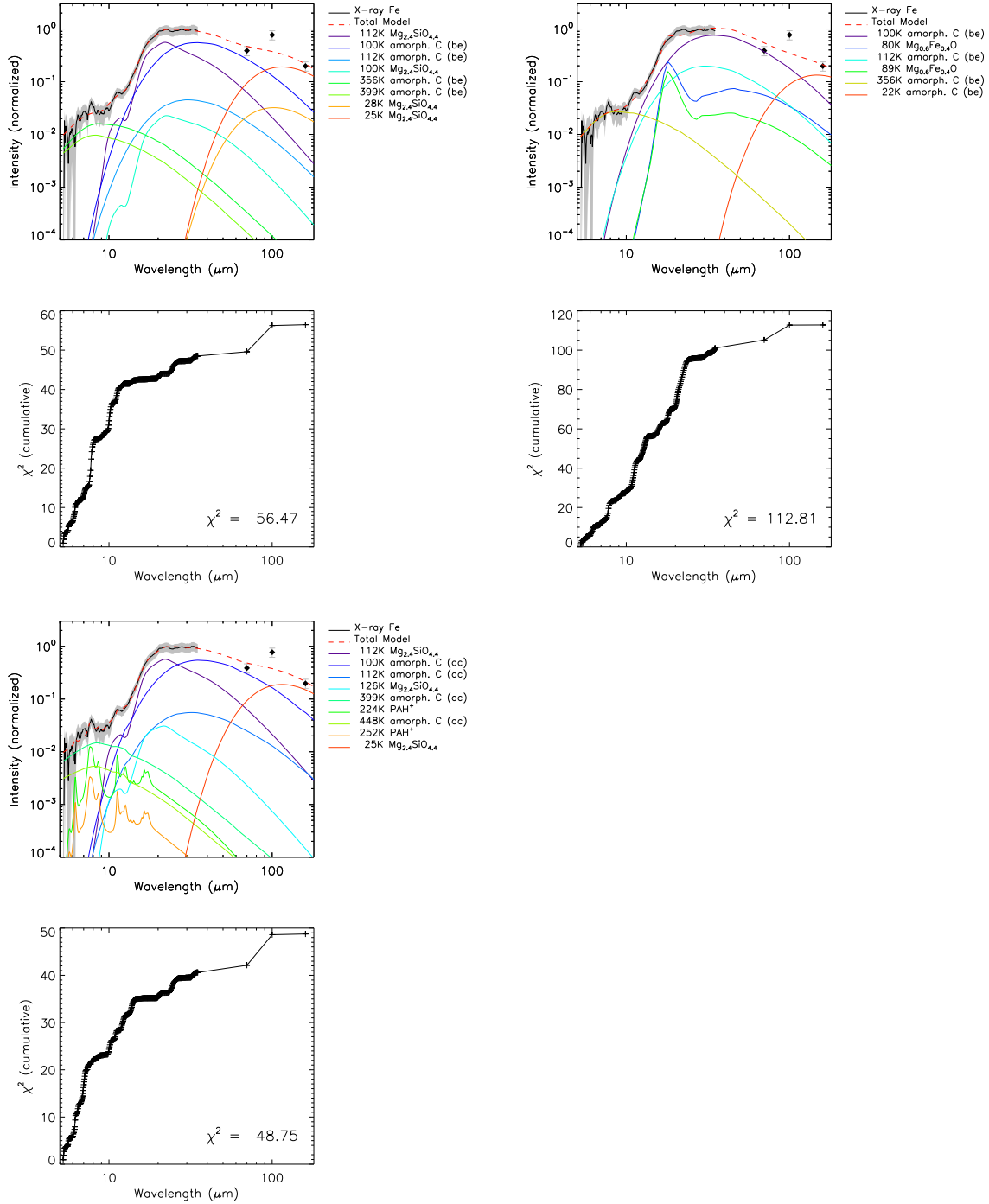


Fig. 17.— (upper left) The best 2-component fit to the X-ray Fe spectrum uses a Mg silicate in combination with a featureless composition. (upper right) This alternate 2-component fit (without silicates) is about a factor of 2 worse than the best fit, and is thus only marginally acceptable. (lower left) The best 3-component fit uses ionized PAHs to match the small (and possibly spurious) bump at  $8 \mu\text{m}$ .

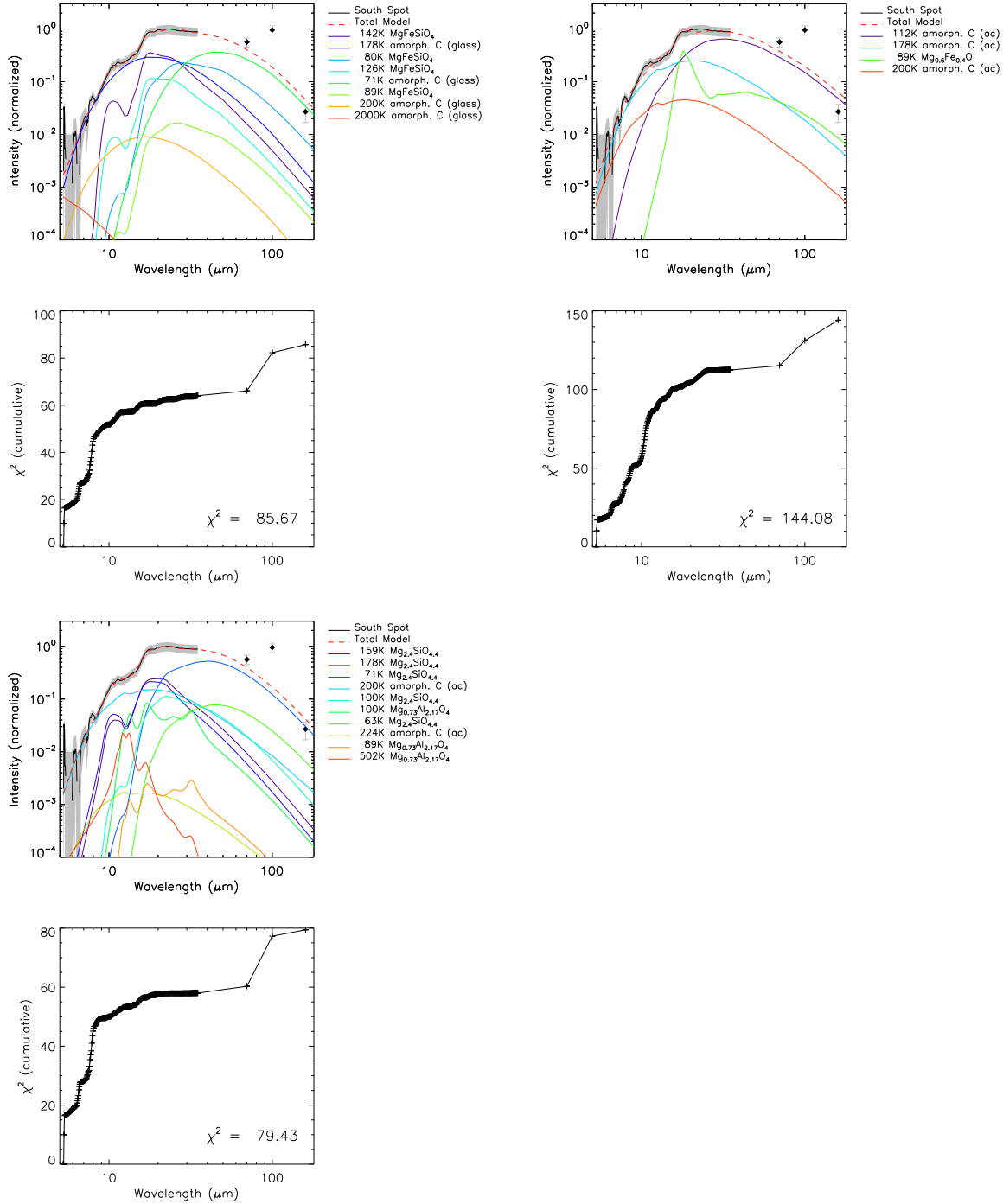


Fig. 18.— (upper left) The best 2-component fits to the South Spot spectrum are similar to those for the X-ray Fe spectrum, but involved higher dust temperatures for the dominant components. (upper right) An alternate 2-component fit again shows that reasonable (though worse) fits can also be obtained without the use of silicates. (lower left) The best 3-component fit uses nonstoichiometric spinel as a third component to make relatively minor adjustments to the model.

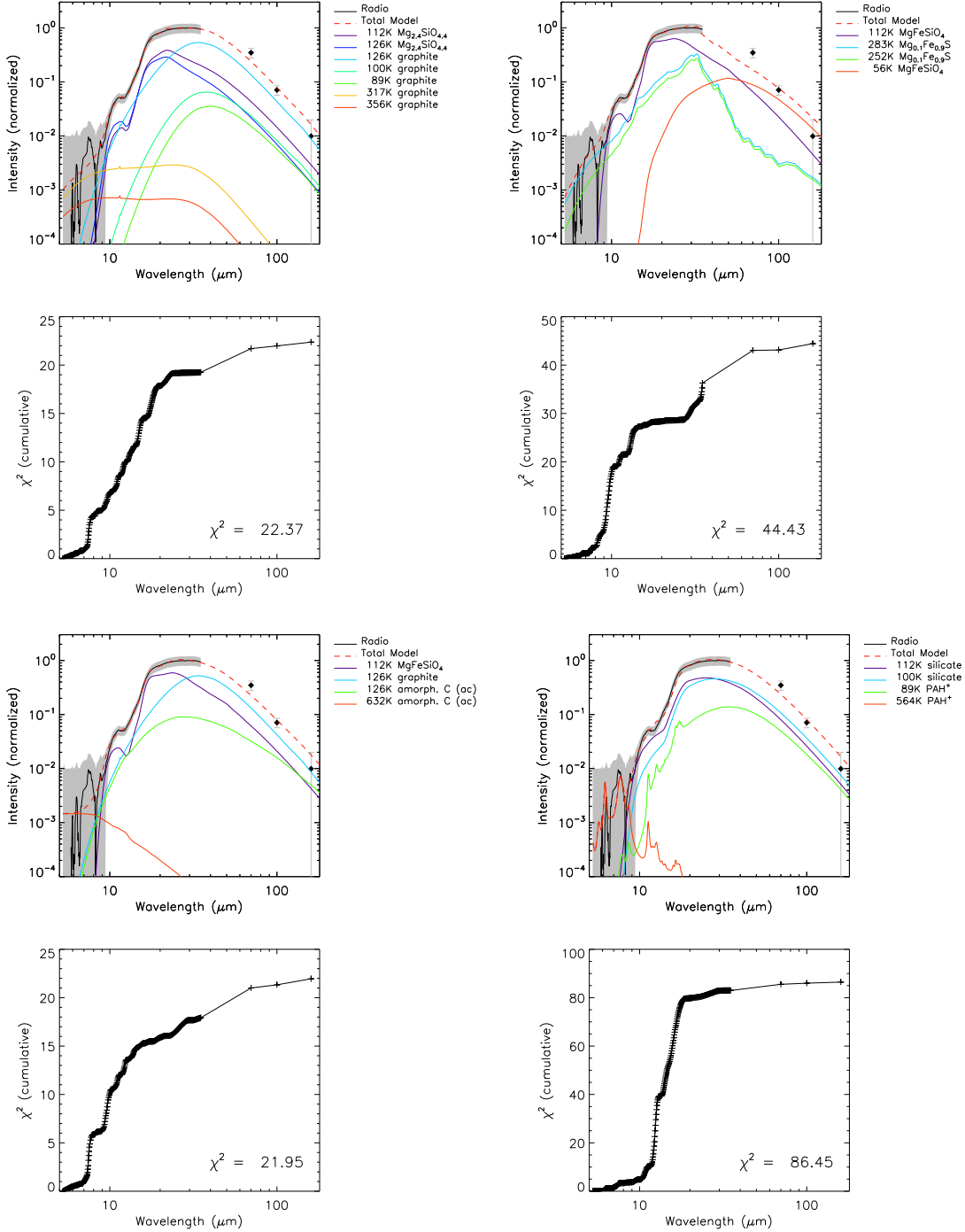


Fig. 19.— (upper left) The best 2-component fit to the Radio spectrum uses graphite and a Mg silicate. Combinations of other silicates with other featureless components are nearly as good. (upper right) This alternate fit to the Radio spectrum shows a marginal model using a sulfide composition instead of a one of the more featureless dust compositions. (lower left) The best 3-component fit is only very slightly better than the 2-component fit. (lower right) The fit using the standard astronomical silicate, graphite, PAH, and PAH<sup>+</sup> combination. Only two of the four components are actually needed for the fit since the PAH<sup>+</sup> component is sufficient to provide a relatively featureless component at  $\gtrsim 20 \mu\text{m}$  and the PAH emission band at  $\sim 8 \mu\text{m}$ .

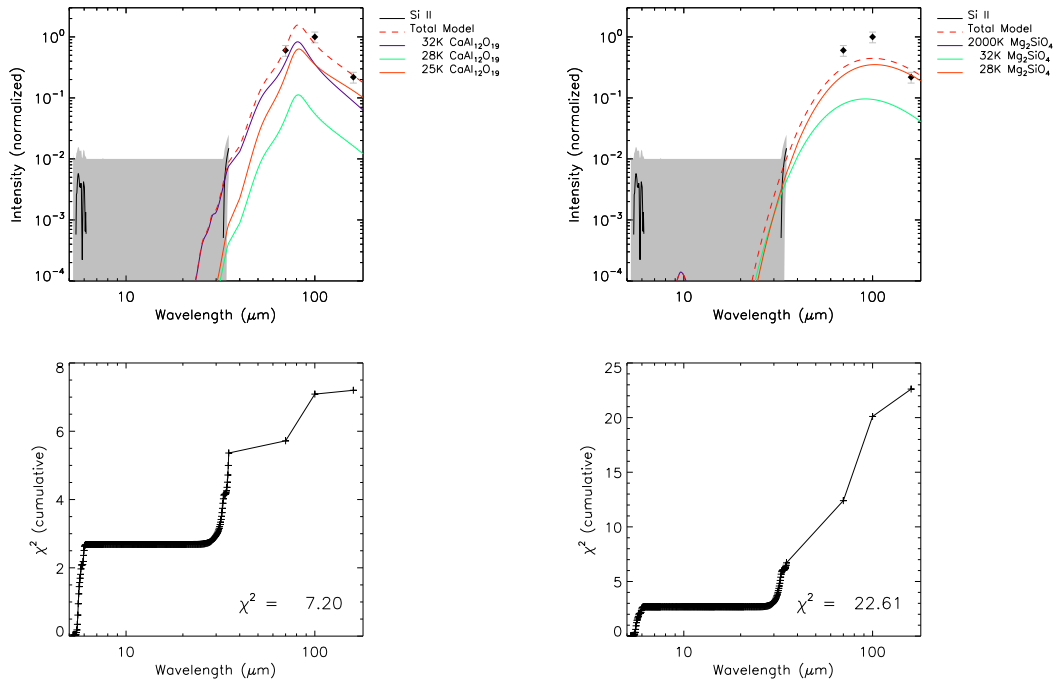


Fig. 20.— (left) The best 1-component fit to the Si II spectrum uses  $\text{CaAl}_{12}\text{O}_{19}$ , which happens to have a broad peak in its absorption efficiency at  $\sim 80 \mu\text{m}$  (right) This alternate fit uses  $\text{Mg}_2\text{SiO}_4$  which has a more typical power law absorption efficiency with an index of  $-2$  at long wavelengths.

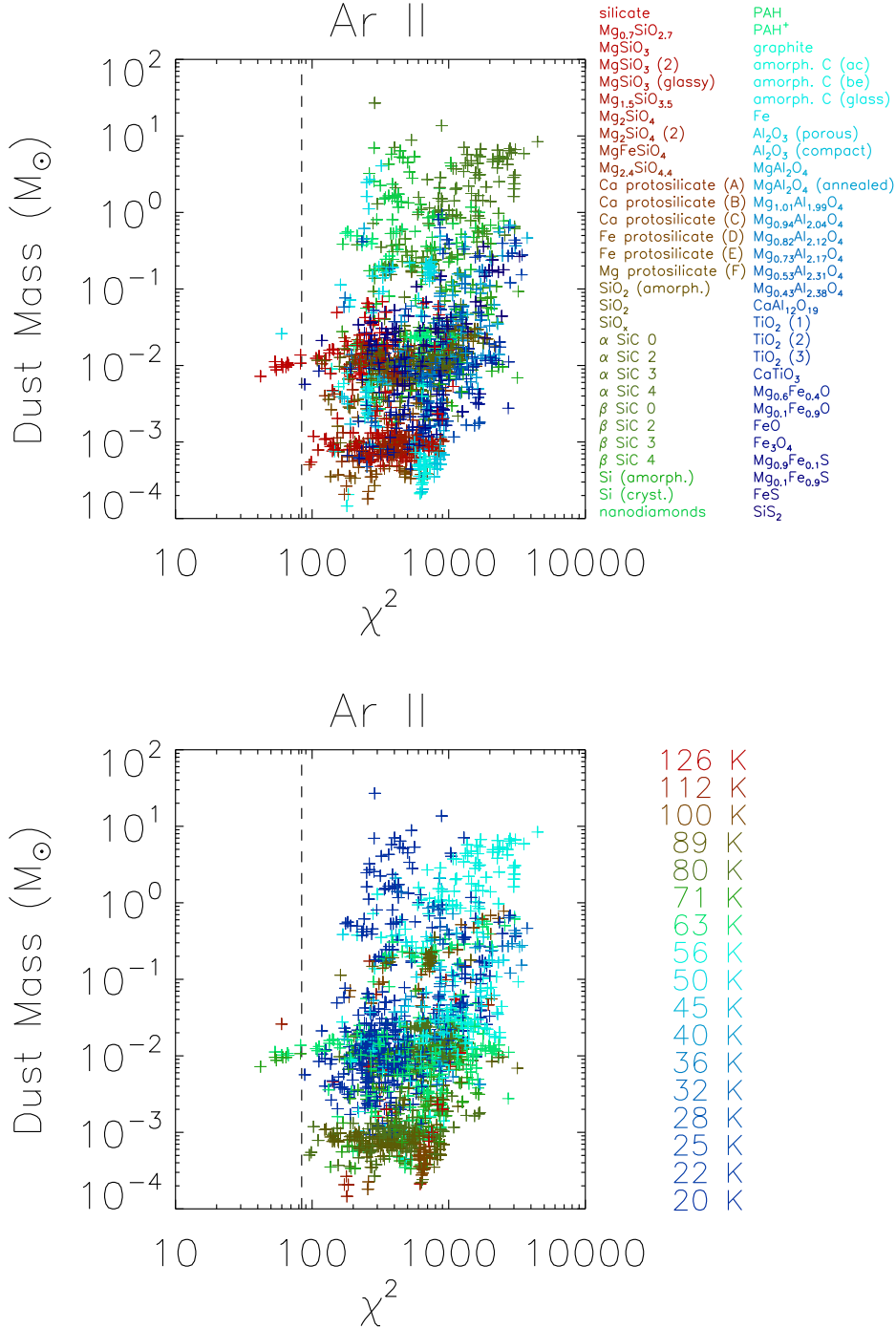


Fig. 21.— Total dust masses for Ar II models. In the top panel the points are color coded by the composition that provides the largest mass component. In the bottom panel the masses are color coded by the temperature of the dominant mass component. Only models to the left of the dashed line (within a factor of 2 in  $\chi^2$  of the best model) are deemed acceptable. These good models indicate that  $\sim 10^{-2} M_{\odot}$  of dust, mostly silicates at  $\sim 70K$ , is associated with the Ar II emission in Cas A.

Table 1. Linear Correlation Coefficients between the Spatial Templates

	<b>[Ar II]</b>	<b>[Ar III]</b>	[S IV]	[Ne V]	[Fe II]	[S III]	IRAC 8 $\mu\text{m}$	<b>[Ne II]</b>	[Ne III]	IRAC 4.5 $\mu\text{m}$	[O IV]	[S II]	<b>[Si II]</b>	<b>X-ray Fe</b>	X-ray Si	<b>Radio</b>
[Ar II] 6.99 $\mu\text{m}$	1.00	0.99	0.97	0.89	0.77	0.97	0.97	0.76	0.76	0.88	0.83	0.84	0.54	0.44	0.67	0.54
[Ar III] 8.99 $\mu\text{m}$	...	1.00	0.97	0.88	0.78	0.95	0.97	0.73	0.73	0.87	0.82	0.83	0.56	0.46	0.68	0.54
[S IV] 10.51 $\mu\text{m}$	...	...	1.00	0.85	0.74	0.96	0.93	0.74	0.75	0.84	0.88	0.89	0.66	0.41	0.65	0.55
[Ne V] 14.32 $\mu\text{m}$	...	...	...	1.00	0.73	0.90	0.85	0.78	0.81	0.84	0.82	0.82	0.56	0.45	0.65	0.53
[Fe II] 17.94 $\mu\text{m}$	...	...	...	...	1.00	0.74	0.76	0.58	0.61	0.73	0.67	0.65	0.45	0.34	0.48	0.45
[S II] 18.71 $\mu\text{m}$	...	...	...	...	...	1.00	0.92	0.77	0.79	0.85	0.88	0.90	0.64	0.46	0.70	0.58
IRAC 8 $\mu\text{m}$	...	...	...	...	...	...	1.00	0.70	0.70	0.87	0.75	0.76	0.45	0.43	0.63	0.47
[Ne II] 12.81 $\mu\text{m}$	...	...	...	...	...	...	...	1.00	0.96	0.90	0.81	0.73	0.50	0.37	0.50	0.48
[Ne III] 15.56 $\mu\text{m}$	...	...	...	...	...	...	...	...	1.00	0.88	0.83	0.75	0.54	0.42	0.52	0.50
IRAC 4.5 $\mu\text{m}$	...	...	...	...	...	...	...	...	...	1.00	0.81	0.76	0.49	0.45	0.58	0.54
[O IV] 25.89 $\mu\text{m}$	...	...	...	...	...	...	...	...	...	...	1.00	0.93	0.83	0.39	0.64	0.62
[S II] 33.48 $\mu\text{m}$	...	...	...	...	...	...	...	...	...	...	...	1.00	0.84	0.41	0.62	0.62
[Si II] 34.82 $\mu\text{m}$	...	...	...	...	...	...	...	...	...	...	...	...	1.00	0.23	0.42	0.55
X-ray Fe	...	...	...	...	...	...	...	...	...	...	...	...	...	1.00	0.71	0.65
X-ray Si	...	...	...	...	...	...	...	...	...	...	...	...	...	...	1.00	0.75
Radio	...	...	...	...	...	...	...	...	...	...	...	...	...	...	...	1.00

Note. — Spatial templates in boldface were selected as the basis for further analysis.



Table 2. Chosen Spatial Templates

Template	Purpose
[Ar II]	trace dust in the most dominant line emitting ejecta
[Ne II]	trace dust in a distinctly different ejecta component from higher layers of the SN
X-ray Fe	trace dust in hotter, low-density ejecta from the inner portion of the SN
Radio	trace ISM or CSM dust swept up behind the forward shock
[Si II]	trace dust in slow-moving ejecta, yet to cross the reverse shock
[Ar III]	test if dust properties differ in regions where ionization state of the gas is higher

Table 3. Dust Compositions Considered for Fitting Spectra

$n$	Composition	$\lambda$ Range ( $\mu\text{m}$ )	Note	Reference
Silicates				
0	Silicate	0.01–9400		Draine & Lee (1984)
1	$\text{Mg}_{0.7}\text{SiO}_{2.7}$	0.2–470		Jäger et al. (2003)
2	$\text{MgSiO}_3$	0.2–10000		Jäger et al. (2003)
3	$\text{MgSiO}_3$	0.1–100000		Dorschner et al. (1995); Kozasa (priv. comm.)
4	$\text{MgSiO}_3$	0.2–500	glassy	Jaeger et al. (1994); Dorschner et al. (1995)
5	$\text{Mg}_{1.5}\text{SiO}_{3.5}$	0.2–6000		Jäger et al. (2003)
6	$\text{Mg}_2\text{SiO}_4$	0.2–950		Jäger et al. (2003)
7	$\text{Mg}_2\text{SiO}_4$	0.1–100000		Jäger et al. (2003); Kozasa (priv. comm.)
8	$\text{MgFeSiO}_4$	0.2–500	glassy	Jaeger et al. (1994); Dorschner et al. (1995)
9	$\text{Mg}_{2.4}\text{SiO}_{4.4}$	0.2–8200		Jäger et al. (2003)
Protosilicates				
10	Ca Protosilicate	7.6–25	A – unheated	Dorschner et al. (1980)
11	Ca Protosilicate	7.7–25	B – 450C	Dorschner et al. (1980)
12	Ca Protosilicate	7.8–25	C – 695C	Dorschner et al. (1980)
13	Fe Protosilicate	8.2–40	D – unheated	Dorschner et al. (1980)
14	Fe Protosilicate	8–40	E – 490C	Dorschner et al. (1980)
15	Mg Protosilicate	8–40	F – 485C	Dorschner et al. (1980)
Silica				
16	$\text{SiO}_2$	0.1–500	am	Philipp (1985); Kozasa (priv. comm.)
17	$\text{SiO}_2$	5–500		Philipp (1985)
18	$\text{SiO}_x$	5.6–520	extrap. at $\lambda > 65 \mu\text{m}$	Rinehart et al. (2011)
SiC, Si				
19	$\alpha$ SiC	0.1–1000	$21 \mu\text{m} : Q_{abs}/a = 0$	Jiang et al. (2005)
20	$\alpha$ SiC	0.1–1000	$21 \mu\text{m} : Q_{abs}/a = 100$	Jiang et al. (2005)
21	$\alpha$ SiC	0.1–1000	$21 \mu\text{m} : Q_{abs}/a = 10^3$	Jiang et al. (2005)
22	$\alpha$ SiC	0.1–1000	$21 \mu\text{m} : Q_{abs}/a = 10^4$	Jiang et al. (2005)
23	$\beta$ SiC	0.1–1000	$21 \mu\text{m} : Q_{abs}/a = 0$	Jiang et al. (2005)
24	$\beta$ SiC	0.1–1000	$21 \mu\text{m} : Q_{abs}/a = 100$	Jiang et al. (2005)
25	$\beta$ SiC	0.1–1000	$21 \mu\text{m} : Q_{abs}/a = 10^3$	Jiang et al. (2005)
26	$\beta$ SiC	0.1–1000	$21 \mu\text{m} : Q_{abs}/a = 10^4$	Jiang et al. (2005)
27	Si	0.02–247.7	am	Piller (1985); Kozasa (priv. comm.)
28	Si	0.07–433.3	cr	Edwards (1985); Kozasa (priv. comm.)
C, Fe				
29	Meteoritic Diamond	0.02–110		Braatz et al. (2000); Mutschke et al. (2004)
30	PAH	0.01–9400		Draine & Li (2007)
31	$\text{PAH}^+$	0.01–9400		Draine & Li (2007)
32	Graphite	0.01–9400		Draine & Lee (1984)

Table 3—Continued

$n$	Composition	$\lambda$ Range ( $\mu\text{m}$ )	Note	Reference
33	Carbon	0.01–9400	amorphous “ac”	Rouleau & Martin (1991)
34	Carbon	0.01–9400	amorphous “be”	Rouleau & Martin (1991)
35	Carbon	0.1–3000	glass	Edoh (1983); Kozasa (priv. comm.)
36	Fe	0.1–100000		Lynch & Hunter (1991); Kozasa (priv. comm.)
Al Oxides				
37	$\text{Al}_2\text{O}_3$	7.8–500	porous	Begemann et al. (1997)
38	$\text{Al}_2\text{O}_3$	7.8–200	compact	Begemann et al. (1997)
Oxides				
39	$\text{MgAl}_2\text{O}_4$	2–10000	natural	Fabian et al. (2001)
40	$\text{MgAl}_2\text{O}_4$	2–6800	natural, annealed	Fabian et al. (2001)
41	$\text{Mg}_{1.01}\text{Al}_{1.99}\text{O}_4$	1.67–6825	nonstoich. spinel	Zeidler et al. (2011)
42	$\text{Mg}_{0.94}\text{Al}_{2.04}\text{O}_4$	1.67–6825	nonstoich. spinel	Zeidler et al. (2011)
43	$\text{Mg}_{0.82}\text{Al}_{2.12}\text{O}_4$	1.67–6825	nonstoich. spinel	Zeidler et al. (2011)
44	$\text{Mg}_{0.73}\text{Al}_{2.17}\text{O}_4$	1.67–6825	nonstoich. spinel	Zeidler et al. (2011)
45	$\text{Mg}_{0.53}\text{Al}_{2.31}\text{O}_4$	1.67–6825	nonstoich. spinel	Zeidler et al. (2011)
46	$\text{Mg}_{0.43}\text{Al}_{2.38}\text{O}_4$	2–10000	nonstoich. spinel	Zeidler et al. (2011)
47	$\text{CaAl}_{12}\text{O}_{19}$	2–10000	hibonite	Mutschke et al. (2002)
48	$\text{TiO}_2$ (1)	2–5843	anatase	Posch et al. (2003); Zeidler et al. (2011)
49	$\text{TiO}_2$ (2)	2–5843	brookite	Posch et al. (2003); Zeidler et al. (2011)
50	$\text{TiO}_2$ (3)	0.47–36	rutile	Posch et al. (2003); Zeidler et al. (2011)
51	$\text{CaTiO}_4$	2–5820	perovskite	Posch et al. (2003); Zeidler et al. (2011)
52	$\text{Mg}_{0.6}\text{Fe}_{0.4}\text{O}$	0.2–500		Henning et al. (1995)
53	$\text{Mg}_{0.1}\text{Fe}_{0.9}\text{O}$	0.2–500		Henning et al. (1995)
54	FeO	0.2–500		Henning et al. (1995)
55	$\text{Fe}_3\text{O}_4$	0.1–100000		Mukai (1989); Kozasa (priv. comm.)
Sulfides				
56	$\text{Mg}_{0.9}\text{Fe}_{0.1}\text{S}$	10–500		Begemann et al. (1994)
57	$\text{Mg}_{0.1}\text{Fe}_{0.9}\text{S}$	10–500		Begemann et al. (1994)
58	FeS	0.1–100000		Semenov et al. (2003); Kozasa (priv. comm.)
59	$\text{SiS}_2$	13–60		Begemann et al. (1996)

Table 4. Best 2-Composition Fits of Cas A Dust

Spectrum	Compositions <sup>1</sup>	Total Dust Mass ( $M_{\odot}$ ) <sup>2</sup>
Ar II	<b>Mg<sub>0.7</sub>SiO<sub>2.7</sub></b> + [Graphite    C (ac)    FeS    C (glass)    Fe    C (be)    Al <sub>2</sub> O <sub>3</sub>    Mg <sub>x</sub> Al <sub>y</sub> O <sub>4</sub>    Fe <sub>3</sub> O <sub>4</sub> ]	0.01 ± 0.002
Ar III	<b>Mg<sub>0.7</sub>SiO<sub>2.7</sub></b> + [Mg <sub>x</sub> Al <sub>y</sub> O <sub>4</sub>    C (ac)    Al <sub>2</sub> O <sub>3</sub>    C (glass)    Fe    C (be)    Graphite    CaAl <sub>12</sub> O <sub>19</sub>    Fe <sub>3</sub> O <sub>4</sub> ]	0.004 ± 0.001
Ne II	<b>Al<sub>2</sub>O<sub>3</sub></b> + [C (be)    C (ac)    C (glass)    Fe    Graphite    FeS    Fe <sub>3</sub> O <sub>4</sub>    Mg <sub>0.1</sub> Fe <sub>0.9</sub> S]	0.004 ± 0.001
X-ray Fe	<b>Mg<sub>2.4</sub>SiO<sub>4.4</sub></b> + [C (be)    C (glass)    Fe    Mg <sub>0.1</sub> Fe <sub>0.9</sub> S    C (ac)    Graphite    FeS    Fe <sub>3</sub> O <sub>4</sub> ] <b>MgFeSiO<sub>4</sub></b> + [C (be)    C (glass)    Fe    Mg <sub>0.1</sub> Fe <sub>0.9</sub> S    C (ac)]	0.02 ± 0.01
South Spot	<b>MgFeSiO<sub>4</sub></b> + [C (glass)    C (ac)    C (be)    Fe] <b>Mg<sub>2.4</sub>SiO<sub>4.4</sub></b> + [C (ac)    Fe    C (be)    C (glass)]	0.0001 ± 3 × 10 <sup>-5</sup>
Radio	<b>Mg<sub>2.4</sub>SiO<sub>4.4</sub></b> + [Graphite    Mg <sub>x</sub> Al <sub>y</sub> O <sub>4</sub>    Mg <sub>0.1</sub> Fe <sub>0.9</sub> S    C (glass)    PAH <sup>+</sup>    Al <sub>2</sub> O <sub>3</sub>    FeS    Fe    C (be)] <b>MgFeSiO<sub>4</sub></b> + [Graphite    C (glass)    Al <sub>2</sub> O <sub>3</sub>    Fe    C (be)    FeS    Mg <sub>0.1</sub> Fe <sub>0.9</sub> S]	0.0004 ± 0.0004
Si II	Indeterminate	≲ 0.1

<sup>1</sup>The compositions in **bold** need to be paired with any *one* of the generally more featureless components listed after the “+” sign (i.e. || indicates “or”). These components are listed in order of increasing  $\chi^2$ , but the differences are not significant.

<sup>2</sup>Mean and  $\sigma$  for good models in which the bold components at left are the dominant mass.

Table 5. Possible Compositions for the 12  $\mu\text{m}$  Peak of Ar II, Ar III Dust

Compositions	Comment
SiO <sub>2</sub>	requires CDE calculation of $\kappa_\lambda$ , also contributes to 9 and 21 $\mu\text{m}$ features
SiC	requires CDE calculation of $\kappa_\lambda$
Mg <sub>x</sub> Al <sub>y</sub> O <sub>4</sub>	requires extremely high temperatures ( $> 2000$ K) [ $y = (8 - 2x)/3$ ]
CaAl <sub>12</sub> O <sub>19</sub>	requires extremely high temperatures ( $> 2000$ K)